

# The effect of material orientation on void growth

N. Hosseini, J. C. Nieto-Fuentes\*, M. Dakshinamurthy, J. A. Rodríguez-Martínez, G. Vadillo

*Department of Continuum Mechanics and Structural Analysis. University Carlos III of Madrid. Avda. de la Universidad, 30. 28911 Leganés, Madrid, Spain*

---

## Abstract

In this work, we have brought to light the effect of material orientation on void growth. For that purpose, we have performed finite element calculations using a cubic unit-cell model with a spherical void at its center and subjected to periodic boundary conditions. The behavior of the material is described with an elastic isotropic, plastic orthotropic constitutive model with yielding defined by Yld2004-18p criterion (Barlat et al., 2005). We have used the multi-point constraint subroutine developed by Dakshinamurthy et al. (2021) to enforce constant values of macroscopic stress triaxiality  $T$  and Lode parameter  $L$  in calculations that have been carried out for different stress states resulting from the combination of  $T = 0.33, 1$  and  $2$ , with  $L = -1, 0$  and  $1$  (axisymmetric tension, generalized shear and axisymmetric compression, respectively). Firstly, we have performed numerical simulations in which the loading directions are collinear with the orthotropy axes of the material, so that the principal directions of macroscopic stress and strain are parallel. Investigation of the cases for which the minor loading axis coincides either with the rolling, the transverse or the normal direction, has shown that the initially spherical void turns into an ellipsoid whose rate of growth and eccentricity depend on both stress state and material orientation. A key result is that for specific material orientations the anisotropy switches the effect of Lode parameter on void growth, reversing the trends obtained for isotropic von Mises materials. Secondly, we have carried out calculations using a novel strategy which consists of including angular misalignments within the range  $0^\circ \leq \theta \leq 90^\circ$ , so that one loading direction is parallel to one of the symmetry axes of the material, and  $\theta$  is the angle formed between the other two loading directions and the second and third orthotropy axes. In fact, to the authors' knowledge, these are the first unit-cell calculations ever reported in which the material is modeled using a macroscopic anisotropic yield function with prescribed misalignment between loading and material axes and, at the same time, the macroscopic stress triaxiality and the Lode parameter are controlled to be constant during loading. The finite element calculations have shown that the misalignment between loading and material axes makes the void and the faces of the unit-cell to rotate and twist during loading. Moreover, the main contribution of this work is the identification of an intermediate value of the angle  $\theta$  for which the growth rate of the void reaches an extreme value (minimum or maximum), so that the numerical results indicate that material orientation and angular misalignment can be strategically exploited to control void growth, and thus promote or delay localization and fracture of anisotropic

---

\*Corresponding author. Tel. +34 916249588; Fax: +34 916249430. E-mail address:junietof@ing.uc3m.es

30 metal products. The conclusions of this research have been shown to be valid for three different materials (aluminum  
31 alloys 2090-T3, 6111-T4 and 6013) and selected comparisons have also been performed using two additional yield criteria  
32 (CPB06ex2 and Yld2011-27p).

33 *Keywords:*

34 Anisotropy, Material orientation, Void growth, Stress triaxiality, Lode parameter, Unit-cell calculations.

---

## 35 1. Introduction

36 Most structural metallic alloys display plastic anisotropy. Experimental evidence of the anisotropic behavior of metals  
37 was extensively discussed by Benzerga et al. (2004a), Fourmeau et al. (2013), Khadyko et al. (2019) and Benzerga et al.  
38 (2019), among others. Generally, the main sources of anisotropic behavior and failure in metals are considered to be:  
39 (1) plastic anisotropy resulting from the crystallographic texture, (2) topological anisotropy originated from the spatial  
40 distribution of voids and second phase particles and (3) morphological anisotropy, coming from the shape and orientation  
41 of voids and particles. Non-random distribution of crystal orientations (texture) is developed, for instance, in extruded  
42 profiles and rolled plates. In order to model the plastic behavior of these components, the assumption of isotropy is  
43 inadequate and the use of suitable anisotropic constitutive models is essential (Banabic et al., 2000; Abedrabbo et al.,  
44 2007). At the continuum scale, plastic anisotropy is the result of the distortion of the yield surface shape due to the  
45 material micro-structural state.

46 Significant efforts have been made over the years to describe the plastic behavior of isotropic and anisotropic metallic  
47 materials via different kinds of yield functions. For isotropic materials, von Mises (1913, 1928) established a quadratic  
48 yield function, which is still widely used today in industry and academia. However, many face-centered-cubic materials,  
49 such as some aluminum alloys, while may be isotropic, display a constitutive behavior which is better described by  
50 non-quadratic yield surfaces. For instance, Hershey (1954) and Hosford (1972) proposed non-quadratic isotropic yield  
51 functions with a variable exponent that considers the material's crystallographic structure. On the other hand, one of  
52 the first anisotropic yield functions for orthotropic materials was proposed by Hill (1948). The criterion of Hill (1948),  
53 which is quadratic in stresses and contains six independent parameters to describe the state of anisotropy, was later  
54 revisited by himself (Hill, 1979, 1993) to correct what he referred to as *inevitable limitations in the range of validity*  
55 *of the 1948 prototype*. Nevertheless, the popularity of the Hill48 model persists nowadays due to its simplicity and  
56 extensive implementation in commercial finite element codes.

57 Many yield functions have been developed over the years to improve the formulations of Hill (1948, 1979, 1993).  
58 For instance, Barlat and Lian (1989) modified the isotropic model of Hosford (1972) to include in-plane anisotropy.  
59 Later, Barlat et al. (1991, 1997, 2003, 2005) introduced a family of non-quadratic yield functions which use fourth

60 order tensors as linear multiplicative operators acting on the stress tensor to introduce material anisotropy. The linear  
61 transformation approach provides extended flexibility to the yield functions to capture the behaviour of materials with  
62 complex anisotropic response by tailoring the number of anisotropy coefficients, while ensuring the convexity of the  
63 yield surface (Barlat et al., 1991; Karafillis and Boyce, 1993; Barlat et al., 1997, 2003; Bron and Besson, 2004). For  
64 instance, using two linear transformations, Barlat et al. (2005) formulated the so-called Yld2004-13p and Yld2004-  
65 18p yield criteria. These two anisotropic models were derived from different isotropic criteria and contain 13 and 18  
66 anisotropic parameters, respectively. In particular, the Yld2004-18p criterion has been widely used to describe the  
67 main features of the anisotropic behaviour of different grades of aluminum alloys (Yoon et al., 2006; Achani et al.,  
68 2009; Fourmeau et al., 2011; Achani et al., 2011; Tardif and Kyriakides, 2012). Years later, Aretz and Barlat (2013)  
69 derived the so-called Yld2011-18p and Yld2011-27p criteria, which use two and three linear transformations of the stress  
70 deviator, respectively, and involve a total of 18 and 27 anisotropic parameters. However, while using multiple linear  
71 transformations enables to construct more flexible and accurate yield functions, the increase in the number of material  
72 parameters requires a larger number of experiments for the calibration of the yield criteria, and the implementation in  
73 finite element codes becomes more laborious and generally less efficient.

74 Ductile fracture of metals and alloys has been subject to many studies over the past decades and is known to occur  
75 by nucleation, growth or enlargement of voids and final void coalescence. The voids in the material either preexist  
76 (Toda et al., 2004), or nucleate at material second phase particles due to decohesion of the particle-matrix interface,  
77 or by particle fracture (Maire et al., 2011). Once the voids nucleate, further plastic deformation enlarges the void size  
78 and distorts its shape. During the course of stable deformation, as voids evolve, plastic strain is more or less uniformly  
79 distributed in the material. At some point, deformation localizes in a narrow region of the material and adjacent voids  
80 ultimately connect or coalesce with each other.

81 The field of porous plasticity has attracted the attention of many investigators. As recent examples, Torki et al.  
82 (2017) developed a micromechanics-based constitutive model to describe plasticity in solids with relatively high levels of  
83 porosity. The developed model was obtained by limit analysis considering a cylindrical voided cell loaded under combined  
84 tension and shear. Brünig et al. (2018) performed numerical analysis and shear-compression experiments to study the  
85 effect of stress state on damage criteria, with special emphasis on negative stress triaxialities. Torki (2019) proposed  
86 a closed-form yield criterion for void growth and coalescence under combined tension and shear stress conditions and  
87 validated the analytical results using cell-model finite element calculations. Becker and Callaghan (2020) examined a  
88 large population of voids nucleated from randomly distributed spherical particles in order to assess the dependence of  
89 load path and mean stress of void growth behavior. Very recently, Shen et al. (2020) developed a new macroscopic yield  
90 criterion for a porous Drucker-Prager matrix material and validated the obtained analytical results with numerical finite

91 element simulations.

92 Finite element void cell simulations have been widely used for almost the last 50 years (Needleman, 1972; Tvergaard,  
93 1982, 1990; Koplik and Needleman, 1988; Worswick and Pick, 1990; Becker and Smelser, 1994; Kuna and Sun, 1994;  
94 Pardoen and Hutchinson, 2000) to provide useful information about the effect of porous microstructure (void shape,  
95 void volume fraction, relative void spacing), flow properties of the matrix material, and stress state on the physics of  
96 ductile damage. In addition, finite element void cell simulations can offer a basis for assessing the predictive ability of  
97 different constitutive models before applying them to more complex real-world problems. Most void cell calculations  
98 reported in the literature have been performed for isotropic matrix materials and spheroidal voids, where the matrix  
99 material is governed by von Mises yield function (e.g., Faleskog et al. (2000), Pardoen and Hutchinson (2003), Kim et al.  
100 (2004), Benzerga et al. (2004b), Danas and Ponte Castañeda (2012)). Studies dealing with unit-cell simulations involving  
101 plastically anisotropic matrix descriptions have been also reported in the literature, but less often than for isotropic  
102 ductile materials. A notable exception is the work of Benzerga and Besson (2001), who carried out simulations using  
103 axisymmetric unit-cells with Hill (1948) criterion representing the matrix material. On the other hand, three-dimensional  
104 unit-cell simulations with a matrix material obeying Hill (1948) plasticity were conducted by Chien et al. (2001) and  
105 Wang et al. (2004). Steglich et al. (2010) performed 3D unit-cell calculations for an anisotropic matrix material following  
106 the yield criterion developed by Bron and Besson (2004). The influence of void shape and anisotropy on void growth in  
107 different materials was analyzed by Keralavarma and Benzerga (2010) and Keralavarma et al. (2011) using axisymmetric  
108 unit-cells with the matrix material being defined by the Hill48 yield criterion. Very recently, Legarh and Tvergaard  
109 (2018) also employed the Hill48 criterion in 3D unit-cell simulations that aimed at studying the interaction between  
110 initial void spacing, void shape, and plastic anisotropy in void growth evolution in porous media. All these studies  
111 noticed the important effect of the matrix anisotropy in the unit-cell response. Note that the influence of anisotropy  
112 on void growth has been also investigated within the framework of crystal plasticity elsewhere (Wan et al., 2005; Yerra  
113 et al., 2010; Lebensohn and Cazacu, 2012; Han et al., 2013; Srivastava and Needleman, 2015; Dakshinamurthy et al.,  
114 2021).

115 Ductile fracture properties have shown marked dependence on the stress state. The deep influence of stress triaxiality  
116 in the mechanisms of damage and in the failure strain of most metals is known since the pioneering works of Rice and  
117 Tracey (1969) and Gurson (1977). In addition, the third invariant of the stress deviator, generally represented by the  
118 Lode parameter, has been shown to play an important role on ductile fracture, notably for low values of the stress  
119 triaxiality. For large values of the stress triaxiality, the micro-voids contained in the material tend to grow fast and  
120 ductile failure occurs by the large increase of void volume fraction which leads to the coalescence of neighboring voids  
121 (see the reviews by Garrison and Moody (1987), Tvergaard (1990) and Benzerga and Leblond (2010)). On the other

hand, for low values of the stress triaxiality, voids tend to flatten, and the void volume fraction decreases as the voids become microcracks, which rotate and elongate (with significant changes in shape) until the final interaction between neighboring microcracks leads to material fracture. Moreover, several authors performed unit-cell analyses for shear dominated loadings and showed that the voids quickly change their orientation and shape while they start to deform, which is influencing the overall behavior of the porous aggregate, as well as the final failure of the material (McVeigh et al., 2007; Leblond and Mottet, 2008; Scheyvaerts et al., 2011; Nielsen et al., 2012; Tvergaard, 2015).

For isotropic materials, the effect of triaxiality, Lode parameter and void shape can be readily analyzed in 3D cell simulations under prescribed loading conditions where the principal directions of the macro stress are aligned with the axes of the cell and the void. However, for anisotropic matrix materials, the response of the cell also depends on the orientation of the anisotropy axes. Recently, Bryhni Dæhli et al. (2017a) performed 3D unit-cell analyses imposing the external stress state of the cubic cell (macroscopic triaxiality and Lode parameter) and considering that the matrix material is governed by the anisotropic yield criterion Yld2004-18p (Barlat et al., 2005). For the sake of simplicity, and to preclude shear effects in the unit-cell model, the material orthotropy directions were imposed to be collinear with the prescribed loading conditions and with the edges of the cell (i.e., material axes parallel to both the applied stress and cell axes), so that the voids initially spherical turned to be ellipsoidal during loading with semi-axes parallel to the loading directions. The calculations of Bryhni Dæhli et al. (2017a) showed that both the exponent of the yield criterion (exponent that governs the curvature of the yield surface) and the directionality of the plastic properties have an important impact on the mechanical response of the unit-cell. In this paper, we extend the analysis of Bryhni Dæhli et al. (2017a) performing unit-cell simulations (with three different sets of material parameters) in which one loading direction is parallel to one of the symmetry axis of the material while the other two loading directions form an angle  $\theta$  with the second and third orthotropy axes, so that the principal directions of macroscopic stress and strain are not aligned. We have investigated angular misalignments within the range  $0^\circ \leq \theta \leq 90^\circ$ , and showed that the growth rate of the void reaches an extreme value (minimum or maximum) for an intermediate value of the angle  $\theta$ . This conclusion is an original outcome of this paper and it has been substantiated for different values of the stress triaxiality  $T = 0.33, 1$  and  $2$ , and the Lode parameter  $L = -1, 0$  and  $1$ , and for different orientations of the unit-cell in which the major or the minor loading direction coincides either with the rolling, the transverse or the normal direction of orthotropy. Note that, while there are not specific experimental results in the literature to perform a quantitative comparison with the unit-cell finite element calculations presented in this work, some authors have already provided indications on the interplay between plastic anisotropy, material orientation and ductility. The idea is to harness directionality of plastic properties in material design, representing a paradigmatic shift in the way of thinking about the use of plastically anisotropic materials in structural applications. For instance, the influence of plastic anisotropy, yield strength and work hardening

on ductile failure was studied by Frodal et al. (2020) using finite element simulations and strain localization analyses of tensile tests in different material orientations. Finite element calculations were performed in seven in-plane directions, i.e.,  $0^\circ$ ,  $15^\circ$ ,  $30^\circ$ ,  $45^\circ$ ,  $60^\circ$ ,  $75^\circ$  and  $90^\circ$  to the reference direction. The material behavior of the specimen was defined by the Yld2004-18p yield criterion. Plastic anisotropy was found to have a marked influence on the tensile ductility, leading to an important variation in the failure strain with the material orientation, in agreement with the trends observed in the experiments of Khadyko et al. (2014, 2019) and Frodal et al. (2019). Moreover, Basu et al. (2017) determined ductility of Mg alloys using smooth and round notched experimental tensile bars. A simple micromechanical model was proposed to rationalize the tests results, showing that plastic anisotropy could be exploited to aid ductility. Nasim et al. (2019) used an invariant parameter called the Anisotropy Effect on Ductility (AED), earlier proposed by Basu et al. (2017), to tailor the formability of Mg alloys. This invariant parameter, which was proven to correctly portray physical formability measurements, was calculated using tension and compression experimental tests of rolled Mg AZ31 alloy. In order to create a particular AED parameter or formability, an automated inverse optimization strategy was used to predict the routes needed to attain target amount of formability.

The numerical calculations presented in this paper corroborate the results obtained in the works discussed in the paragraph above, and reinforce the idea that material orientation and angular misalignment can be strategically exploited to control void growth, and thus promote or delay localization and fracture of anisotropic metal products. The manuscript is organized as follows. Section 2 presents the elasto-plastic constitutive model used to describe the mechanical behavior of the matrix material. Material yielding is modeled with the Yld2004-18p criterion (Barlat et al., 2005) with parameters corresponding to aluminum alloys 2090-T3, 6111-T4 and 6013. Moreover, Section 3 shows the unit-cell finite element model developed in ABAQUS/Standard (2016), and Section 4 shows calculations in which the principal directions of macroscopic stress and strain are collinear (Section 4.1), and also calculations with prescribed misalignment between the loading and material axes (Section 4.2). A summary of the main findings of the paper is given in Section 5.

## 2. Constitutive framework

We consider an elastic isotropic, plastic orthotropic constitutive model with yielding described by Yld2004-18p criterion (Barlat et al., 2005). This advanced yield criterion is able to successfully describe the main features of the anisotropic behaviour of different grades of aluminum alloys (Fourmeau et al., 2011; Achari et al., 2011; Tardif and Kyriakides, 2012).

The rate of deformation tensor  $\mathbf{d}$  is assumed to be the sum of an elastic part  $\mathbf{d}_e$  and a plastic part  $\mathbf{d}_p$ :

$$\mathbf{d} = \mathbf{d}_e + \mathbf{d}_p \quad (1)$$

182 where the elastic part is related to the rate of the stress by the following linear hypo-elastic law:

$$\overset{\nabla}{\boldsymbol{\sigma}} = \mathbf{L} : \mathbf{d}_e \quad (2)$$

183 where  $\overset{\nabla}{\boldsymbol{\sigma}}$  is an objective derivative of the Cauchy stress tensor (which corresponds to the Jaumann derivative in  
184 ABAQUS/Standard), and  $\mathbf{L}$  is the tensor of isotropic elastic moduli given by:

$$\mathbf{L} = \frac{E}{1 + \nu} \mathbf{I}' + \frac{E}{3(1 - 2\nu)} \mathbf{1} \otimes \mathbf{1} \quad (3)$$

185 with  $E$  being the Young's modulus,  $\nu$  the Poisson's ratio,  $\mathbf{1}$  the unit second-order tensor and  $\mathbf{I}'$  the unit deviatoric  
186 fourth-order tensor.

187

188 The yield function is defined as:

$$\phi = \sum_{i=I}^{III} \sum_{j=I}^{III} |\tilde{s}'_i - \tilde{s}''_j|^a \quad (4)$$

189 where  $\tilde{s}'_i$  and  $\tilde{s}''_j$  are the principal values of the second order deviatoric tensors  $\tilde{\mathbf{s}}'$  and  $\tilde{\mathbf{s}}''$ , which are defined by two linear  
190 transformations:

$$\tilde{\mathbf{s}}' = \mathbf{C}' \mathbf{s} \quad (5a)$$

$$\tilde{\mathbf{s}}'' = \mathbf{C}'' \mathbf{s} \quad (5b)$$

191

192 where  $\mathbf{s}$  is the deviatoric part of the Cauchy stress tensor  $\boldsymbol{\sigma}$ , and  $\mathbf{C}'$  and  $\mathbf{C}''$  are the matrices which contain the anisotropy  
193 coefficients:

$$\mathbf{C}' = \begin{bmatrix} 0 & -c'_{12} & -c'_{13} & 0 & 0 & 0 \\ -c'_{21} & 0 & -c'_{23} & 0 & 0 & 0 \\ -c'_{31} & -c'_{32} & 0 & 0 & 0 & 0 \\ 0 & 0 & 0 & c'_{44} & 0 & 0 \\ 0 & 0 & 0 & 0 & c'_{55} & 0 \\ 0 & 0 & 0 & 0 & 0 & c'_{66} \end{bmatrix} \quad (6a)$$

$$\mathbf{C}'' = \begin{bmatrix} 0 & -c''_{12} & -c''_{13} & 0 & 0 & 0 \\ -c''_{21} & 0 & -c''_{23} & 0 & 0 & 0 \\ -c''_{31} & -c''_{32} & 0 & 0 & 0 & 0 \\ 0 & 0 & 0 & c''_{44} & 0 & 0 \\ 0 & 0 & 0 & 0 & c''_{55} & 0 \\ 0 & 0 & 0 & 0 & 0 & c''_{66} \end{bmatrix} \quad (6b)$$

194

195 with  $c'_{ij}$  and  $c''_{ij}$  being material parameters. Note that in equation (5) we have taken the order of the components  
 196 of the column vector representing the deviatoric stress tensor to be  $\mathbf{s} = \{s_{xx} \ s_{yy} \ s_{zz} \ s_{yz} \ s_{zx} \ s_{xy}\}$ , with the Cartesian  
 197 coordinate system  $(x, y, z)$  being associated to the orthotropy axes of the material ( $x$ ,  $y$  and  $z$  axes correspond to the  
 198 rolling, transverse and normal directions, respectively).

199

200 The ordered principal values of the tensor  $\tilde{\mathbf{s}}'$  are:

$$\tilde{s}'_I = 2\sqrt{(H'_1)^2 + H'_2} \cos\left(\frac{\theta}{3}\right) + H'_1 \quad (7a)$$

$$\tilde{s}'_{II} = 2\sqrt{(H'_1)^2 + H'_2} \cos\left(\frac{\theta + 4\pi}{3}\right) + H'_1 \quad (7b)$$

$$\tilde{s}'_{III} = 2\sqrt{(H'_1)^2 + H'_2} \cos\left(\frac{\theta + 2\pi}{3}\right) + H'_1 \quad (7c)$$

201

202 with  $\theta = \arccos\left(\frac{q}{p^{3/2}}\right)$ ,  $p = (H'_1)^2 + H'_2$  and  $q = \frac{2(H'_1)^3 + 3H'_1H'_2 + 2H'_3}{2}$ , where  $H'_1$ ,  $H'_2$  and  $H'_3$  are the 1<sup>st</sup>, 2<sup>nd</sup> and  
 203 3<sup>rd</sup> invariant of  $\tilde{\mathbf{s}}'$  (Barlat et al., 2005). The same procedure is followed to obtain the principal values of the tensor  $\tilde{\mathbf{s}}''$ .

204

205 The effective stress associated to this yield criterion is:

$$\bar{\sigma} = \left( \frac{\phi}{\xi} \right)^{1/a} \quad (8)$$

206 with  $\xi = 4$ , so that  $\bar{\sigma}$  reduces to the yield stress in the rolling direction (see equation (9)).

207  
208 Moreover, the yield condition is expressed as:

$$f = \bar{\sigma} - \sigma_Y = 0 \quad (9)$$

209 where  $\sigma_Y$  is the yield stress of the material in the rolling direction (direction  $x$ ), which is considered to evolve following  
210 a power-type relation:

$$\sigma_Y = \sigma_0 (\varepsilon_0 + \bar{\varepsilon}_p)^n \quad (10)$$

211 where  $\bar{\varepsilon}_p = \int_0^t \dot{\varepsilon}_p d\tau$  is the effective plastic strain and  $\dot{\varepsilon}_p$  is the effective plastic strain rate. Moreover,  $\sigma_0$ ,  $\varepsilon_0$ , and  $n$  are  
212 material parameters.

213  
214 Assuming an associated plastic flow rule, the plastic part of the rate of deformation tensor is:

$$\mathbf{d}_p = \dot{\lambda} \frac{\partial \bar{\sigma}}{\partial \boldsymbol{\sigma}} \quad (11)$$

215 where  $\dot{\lambda}$  is the rate of plastic multiplier.

216  
217 In addition, the work conjugacy relation:

$$\boldsymbol{\sigma} : \mathbf{d}_p = \bar{\sigma} \dot{\varepsilon}_p \quad (12)$$

Symbol	Property and units	Value
$\rho_0$	Initial density (kg/m <sup>3</sup> )	2700
$G$	Elastic shear modulus (GPa), Eq. (3)	26.92
$K$	Bulk modulus (GPa), Eq. (3)	58.33

Table 1: Initial density and elastic constants for the three aluminium alloys considered in this work: 2090-T3, 6111-T4 and 6013.

218 leads to the identity:

$$\dot{\varepsilon}_p = \dot{\lambda} \quad (13)$$

219 The formulation of the constitutive model is completed with the Kuhn-Tucker loading-unloading conditions:

$$\dot{\lambda} \geq 0, \quad f \leq 0, \quad \dot{\lambda}f = 0 \quad (14)$$

220 and the consistency condition during plastic loading:

$$\dot{f} = 0 \quad (15)$$

221

222 The parameters values of the constitutive model corresponding to aluminium alloys 2090-T3, 6111-T4 and 6013 are  
 223 shown in Tables 1-7. Fig. 1 shows the projections in the deviatoric  $\pi$ -plane of the yield loci, where  $\sigma_I$ ,  $\sigma_{II}$  and  $\sigma_{III}$  are  
 224 the principal values of the tensor  $\boldsymbol{\sigma}$  corresponding to the rolling, transverse and normal directions, respectively. This  
 225 representation of the yield loci makes apparent the anisotropy and the dependence of yielding on material orientation.  
 226 For instance, note that for aluminium alloy 2090-T3 the minimum and maximum yield stresses correspond to uniaxial  
 227 tension in the transverse and normal directions, respectively. On the other hand, notice that the Yld2004-18p criterion  
 228 reduces to isotropic von Mises (1928) plasticity when  $c'_{ij} = c''_{ij} = 1$  and  $a = 2$  (Barlat et al., 2005).

<b>Aluminium alloy 2090-T3</b>		
<b>Strain hardening parameters</b>		
$\sigma_0$	Material parameter (MPa), Eq. (10)	646
$\varepsilon_0$	Material parameter, Eq. (10)	0.025
$n$	Material parameter, Eq. (10)	0.227

Table 2: Strain hardening parameters for aluminium alloy 2090-T3. Data after Yoon et al. (2006) and Cvitanić et al. (2008).

<b>Aluminium alloy 2090-T3</b>								
<b>Anisotropy parameters</b>								
$c'_{12}$	$c'_{13}$	$c'_{21}$	$c'_{23}$	$c'_{31}$	$c'_{32}$	$c'_{44}$	$c'_{55}$	$c'_{66}$
-0.06989	0.93640	0.07914	1.00306	0.524741	1.36318	1.02377	1.06906	0.95432
$c''_{12}$	$c''_{13}$	$c''_{21}$	$c''_{23}$	$c''_{31}$	$c''_{32}$	$c''_{44}$	$c''_{55}$	$c''_{66}$
0.98117	0.47674	0.57531	0.86682	1.14501	-0.07929	1.05166	1.14700	1.40462
<b>Degree of homogeneity of the yield function</b>								
$a$								
8								

Table 3: Yld2004-18p yield criterion. Parameters values for aluminium alloy 2090-T3. Data after Barlat et al. (2005).

<b>Aluminium alloy 6111-T4</b>		
<b>Strain hardening parameters</b>		
$\sigma_0$	Material parameter (MPa), Eq. (10)	503.7
$\varepsilon_0$	Material parameter, Eq. (10)	0
$n$	Material parameter, Eq. (10)	0.233

Table 4: Strain hardening parameters for aluminium alloy 6111-T4. Data after Kim et al. (2010).

<b>Aluminium alloy 6111-T4</b>								
<b>Anisotropy parameters</b>								
$c'_{12}$	$c'_{13}$	$c'_{21}$	$c'_{23}$	$c'_{31}$	$c'_{32}$	$c'_{44}$	$c'_{55}$	$c'_{66}$
0.637630	0.941853	0.693134	1.009620	0.608808	0.730685	1.004578	0.818717	0.616609
$c''_{12}$	$c''_{13}$	$c''_{21}$	$c''_{23}$	$c''_{31}$	$c''_{32}$	$c''_{44}$	$c''_{55}$	$c''_{66}$
1.281632	1.529747	1.184135	1.476191	-0.67124	-0.96936	1.005348	1.018549	1.245460
<b>Degree of homogeneity of the yield function</b>								
$a$								
8								

Table 5: Yld2004-18p yield criterion. Parameters values for aluminium alloy 6111-T4. Data after Kim et al. (2010).

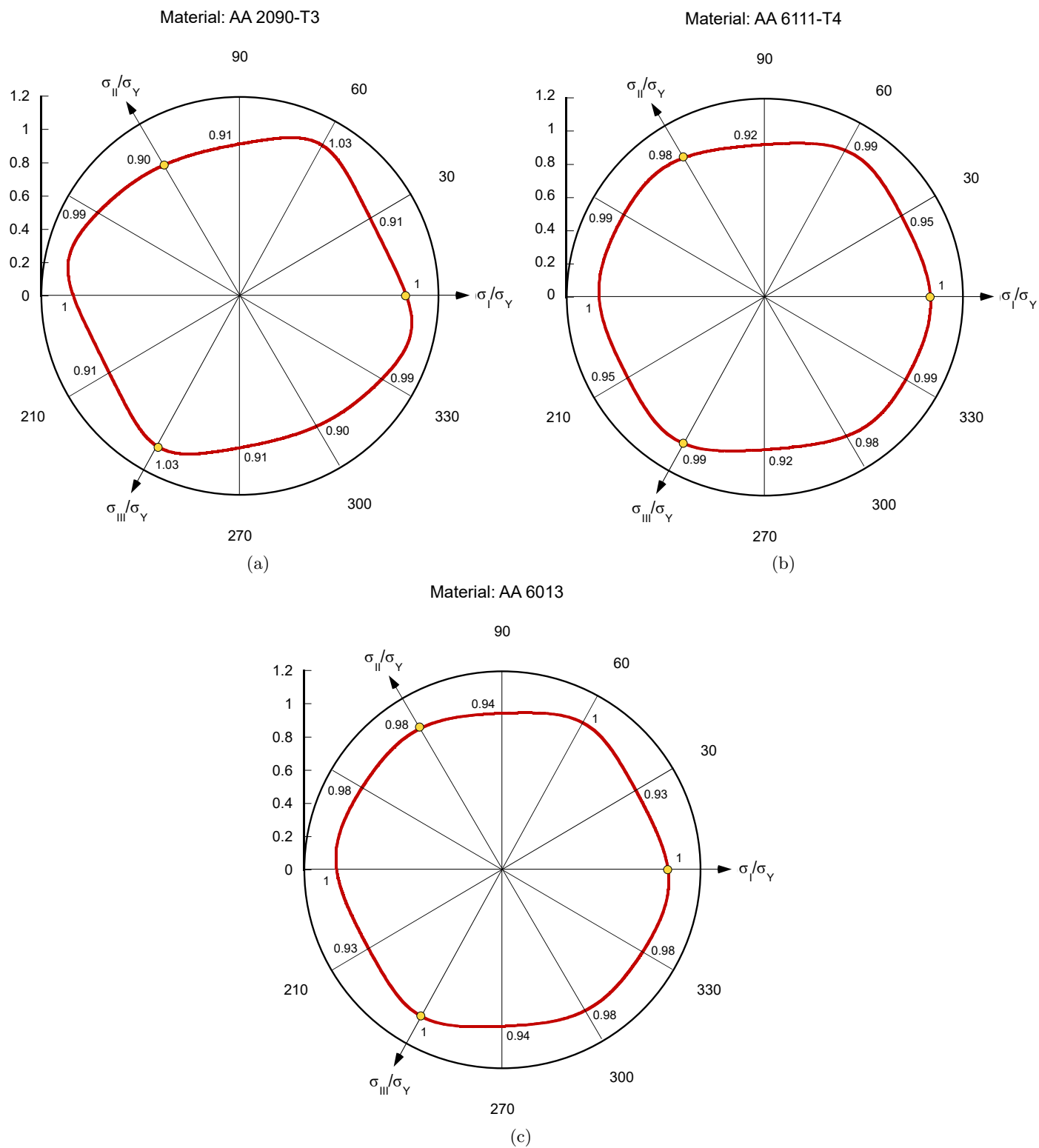


Figure 1: Yld2004-18p yield criterion. Projection in the deviatoric  $\pi$ -plane of the yield locus for aluminium alloys: (a) 2090-T3, (b) 6111-T4 and (c) 6013.

<b>Aluminium alloy 6013</b>		
<b>Strain hardening parameters</b>		
$\sigma_0$	Material parameter (MPa), Eq. (10)	556.06
$\varepsilon_0$	Material parameter, Eq. (10)	0.0062
$n$	Material parameter, Eq. (10)	0.201

Table 6: Strain hardening parameters for aluminium alloy 6013. Data after Ha et al. (2018).

<b>Aluminium alloy 6013</b>								
<b>Anisotropy parameters</b>								
$c'_{12}$	$c'_{13}$	$c'_{21}$	$c'_{23}$	$c'_{31}$	$c'_{32}$	$c'_{44}$	$c'_{55}$	$c'_{66}$
1.0717	1.1541	1.1746	1.1832	0.8482	1.0672	0.9543	1.0142	1.2007
$c''_{12}$	$c''_{13}$	$c''_{21}$	$c''_{23}$	$c''_{31}$	$c''_{32}$	$c''_{44}$	$c''_{55}$	$c''_{66}$
0.8119	0.6928	0.7644	0.6693	1.0239	0.9485	1.0467	0.9846	0.7331
<b>Degree of homogeneity of the yield function</b>								
$a$								
8								

Table 7: Yld2004-18p yield criterion. Parameters values for aluminium alloy 6013. Data after Ha et al. (2018).

### 3. Finite element model

We consider a porous material with periodic microstructure modeled by an array of representative volume elements idealized as cubic unit-cells with a spherical void of initial radius  $R_0 = a_0 = b_0 = c_0$  located at their center, see Fig. 2, where  $a_0$ ,  $b_0$  and  $c_0$  denote the initial radius of the void along the axes  $x_1$ ,  $x_2$  and  $x_3$  (see Section 4.1). The initial size of the cubic cell is  $L_0 \times L_0 \times L_0$ , so that the initial void volume fraction, defined as the ratio between the initial volume of the void and the initial volume of the cell, is  $f_0 = V_0^{void}/V_0^{cell} = 0.0042$ . Moreover, the current volumes of the void and the cell are denoted by  $V^{void}$  and  $V^{cell}$ , respectively, so that the current volume of the matrix material is  $V^{matrix} = V^{cell} - V^{void}$ . The finite element model has been implemented in ABAQUS/Standard (2016), with the initial configuration of the unit cell being defined by the domain  $0 \leq x_1 \leq L_0$ ,  $0 \leq x_2 \leq L_0$  and  $0 \leq x_3 \leq L_0$ . The origin of the Lagrangian Cartesian coordinate system  $(x_1, x_2, x_3)$  is located at the bottom left rear corner of the cell, see Fig. 2. The loading directions are determined by the axes  $x_1, x_2$  and  $x_3$  (see below). The behavior of the matrix material is defined with the constitutive framework presented in Section 2.

We have used the multi-point constraint subroutine developed by Dakshinamurthy et al. (2021) to enforce constant and controlled values of the macroscopic stress triaxiality  $T$  and the macroscopic Lode parameter  $L$  during the calculations. Note that the approach of imposing  $T$  and  $L$  throughout the deformation for the analysis of void growth in

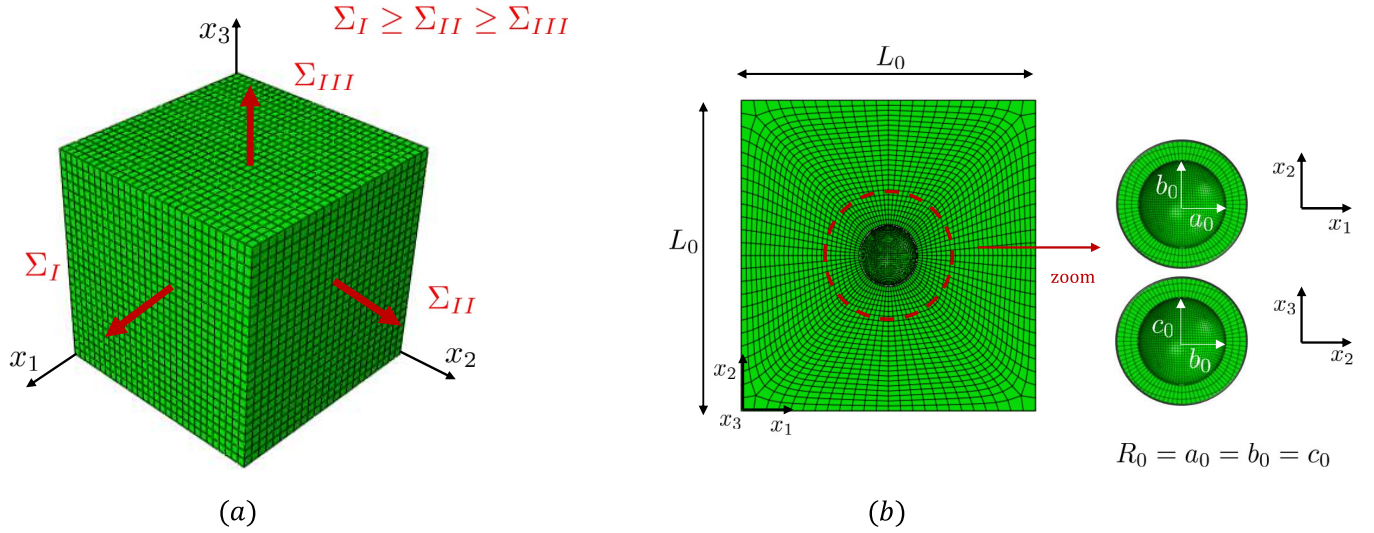


Figure 2: (a) Unit-cell finite element model and (b) cut-view for  $x_3 = \frac{L_0}{2}$  with  $\Sigma_I$ ,  $\Sigma_{II}$  and  $\Sigma_{III}$  being the principal values of the macroscopic stress tensor. The loading directions are aligned with the principal directions of the macroscopic stress tensor, so that the major loading direction corresponds to the principal stress direction associated to  $\Sigma_I$ , and the minor loading direction corresponds to the principal stress direction associated to  $\Sigma_{III}$ .

unit-cell calculations follows from the earlier works of Zhang et al. (2001), Kim et al. (2004), Srivastava and Needleman (2015) and Vadillo et al. (2016), among others. We introduce the macroscopic stress tensor  $\Sigma$  through the following relation with the microscopic (local) Cauchy stress tensor  $\sigma$ :

$$\Sigma = \frac{1}{V^{cell}} \int_{V^{cell}} \sigma dV^{cell} \quad (16)$$

Moreover, the macroscopic effective stress  $\bar{\Sigma}$ , the macroscopic stress triaxiality  $T$  and the macroscopic Lode parameter  $L$  are defined as:

$$\bar{\Sigma} = \sqrt{\frac{3}{2} \Sigma' : \Sigma'}, \quad T = \frac{\Sigma_h}{\bar{\Sigma}}, \quad L = \frac{2\Sigma_{II} - \Sigma_I - \Sigma_{III}}{\Sigma_I - \Sigma_{III}} \quad (17)$$

where:

$$\Sigma' = \Sigma - \Sigma_h \mathbf{1}, \quad \Sigma_h = \frac{\Sigma_I + \Sigma_{II} + \Sigma_{III}}{3} \quad (18)$$

with  $\Sigma_I$ ,  $\Sigma_{II}$  and  $\Sigma_{III}$  being the principal values of the macroscopic stress tensor with  $\Sigma_I \geq \Sigma_{II} \geq \Sigma_{III}$  (i.e.,  $\Sigma_I$ ,  $\Sigma_{II}$  and  $\Sigma_{III}$  are the major, intermediate and minor principal values of the macroscopic stress tensor, respectively). The

loading directions are aligned with the principal directions of the macroscopic stress tensor, so that the major loading direction corresponds to the principal stress direction associated to  $\Sigma_I$  (parallel to  $x_1$ ), and the minor loading direction corresponds to the principal stress direction associated to  $\Sigma_{III}$  (parallel to  $x_3$ ), see Fig. 2.

The volume average of the microscopic (local) logarithmic strain tensor  $\boldsymbol{\epsilon}$ , expressed as:

$$\boldsymbol{\epsilon} = \frac{1}{V^{matrix}} \int_{V^{matrix}} \boldsymbol{\epsilon} dV^{matrix} \quad (19)$$

leads to the macroscopic effective strain  $\bar{\epsilon}$ , as defined by Srivastava and Needleman (2015):

$$\bar{\epsilon} = \sqrt{\frac{2}{3} \boldsymbol{\epsilon}' : \boldsymbol{\epsilon}'}, \quad \boldsymbol{\epsilon}' = \boldsymbol{\epsilon} - \epsilon_h \mathbf{1}, \quad \epsilon_h = \frac{\epsilon_I + \epsilon_{II} + \epsilon_{III}}{3} \quad (20)$$

where  $\epsilon_I$ ,  $\epsilon_{II}$  and  $\epsilon_{III}$  are the principal values of the tensor  $\boldsymbol{\epsilon}$ . Expressions (17) and (20) are scalar measures of macroscopic stress and macroscopic strain, respectively, consistent with the definitions used, for instance, by Srivastava and Needleman (2015), Bryhni Dæhli et al. (2017a) and Dakshinamurthy et al. (2021), in unit-cell calculations analyses with different anisotropic plasticity theories. Note that expressions (17) and (20) do not *determine* the specific effective stress and strain in a material point for this yield criterion —these are given by equations (8) and (12)—, but they are rather used for the definition of macroscopic stress scalars (macroscopic Lode and macroscopic triaxiality) and for the graphical representation and interpretation of results.

In Section 4, we carry out calculations for three different values of macroscopic triaxiality  $T = 0.33, 1$  and  $2$ , and macroscopic Lode parameter  $L = -1, 0$  and  $1$ , and for macroscopic effective strains  $\bar{\epsilon}$  up to  $0.6$ . Similar range of values of macroscopic triaxiality and Lode parameter has been studied elsewhere (e.g., Bryhni Dæhli et al. (2017a,b)). Moreover, recall that  $L = -1, 0$  and  $1$  represent states of axisymmetric tension, generalized shear and axisymmetric compression, respectively. Note that for  $L = -1$  we have that  $\Sigma_I > \Sigma_{II} = \Sigma_{III}$ , for  $L = 0$  the principal values of the macroscopic stress tensor are such that  $\Sigma_I > \Sigma_{II} = \frac{\Sigma_I + \Sigma_{III}}{2} > \Sigma_{III}$ , and for  $L = 1$  we have that  $\Sigma_I = \Sigma_{II} > \Sigma_{III}$ . We are aware that the mechanical behavior of anisotropic materials depends on both the principal stresses and the principal stress directions, so that when presenting the results in Section 4 we always indicate the orientation of the loading axes  $(x_1, x_2, x_3)$  with respect to the material orthotropy directions  $(x, y, z)$ . Note that providing information about the stress eigenvalues and eigenvectors amounts to giving the six independent stress components in arbitrary basis, namely, the basis related to the material orthotropy axes. In this regard, note that in all the calculations performed in this work the

major and minor loading directions are parallel to the  $x_1$  and  $x_3$  axes, respectively. We will further elaborate on this issue in Section 4. In addition, following the procedure described in Appendix A of Dakshinamurthy et al. (2021), we have applied periodic boundary conditions to the unit-cell, ensuring that the relative displacement between opposing nodes is the same (i.e., the displacement of opposing nodes is coupled, e.g., see Fig. 24 in Section 4.2). Moreover, a mesh convergence study showed that a discretization consisting of 86096 eight-node tri-linear elements with reduced integration and hourglass control (C3D8R in ABAQUS notation) yields numerical results for the evolution of the void growth which are virtually mesh independent (for the range of macroscopic effective strains and void volume fractions investigated in this paper). This spatial discretization was used in all the unit-cell simulations performed in this work. Moreover, the elastic-plastic constitutive model presented in Section 2 has been implemented in ABAQUS/Standard (2016) through a UMAT subroutine, using the integration algorithm based on numerical approximation of the yield function gradients developed by Hosseini and Rodríguez-Martínez (2021).

## 4. Results

In Section 4.1, we consider that the loading directions are aligned with the orthotropy axes of the material and investigate the cases for which the minor loading axis  $x_3$  coincides either with the rolling, the transverse or the normal direction (recall that the minor loading direction corresponds to the principal direction associated to  $\Sigma_{III}$ ). The results correspond to AA 2090-T3. Similar calculations were performed by Bryhni Dæhli et al. (2017a) using the Yld2004-18p criterion with parameters corresponding to six generic crystallographic textures representative of different anisotropic face-centered-cubic metals, including brass and copper. In Section 4.2, we investigate the influence of the misalignment between loading and orthotropy axes on void growth, exploring different material orientations. Results are presented for different aluminium alloys: 2090-T3, 6111-T4 and 6013. The main contribution of this paper to the field of finite element void cell calculations is to consider anisotropic materials modeled with a macroscopic yield criterion in which loading and materials axes are not aligned. In addition, for the sake of completeness, Appendix A presents calculations performed with two additional yield criteria, CPB06ex2 (Plunkett et al., 2008) and Yld2011-27p (Aretz and Barlat, 2013), calibrated to model the behavior of AA 2090-T3.

Recall that the loading directions are fixed relative to the Lagrangian coordinate system  $(x_1, x_2, x_3)$  associated to the undeformed cell (see Fig. 2). Moreover, the orthotropy axes  $(x, y, z)$  are associated to the material (locally), with prescribed directions in the undeformed configuration that can rotate if the material rotates during loading (as in the calculations in which loading and material axes are not aligned). The orientation of the orthotropy axes given in the paper corresponds to the undeformed configuration. Moreover, note that we have not included any failure criterion in

the simulations, and we have not analyzed localization of plastic deformation leading to coalescence and subsequent material fracture (the reader is referred to the works of Tekoğlu et al. (2015) and Reboul et al. (2020) where localization and coalescence are analyzed for isotropic materials using unit-cell finite element calculations). The specific influence of plastic anisotropy and material orientation on localization of deformation near the void, coalescence and fracture will be investigated in a future work.

#### 4.1. Alignment between loading and material axes

We perform a parametric analysis on the influence of macroscopic stress triaxiality (Section 4.1.1), Lode parameter (Section 4.1.2) and material orientation (Section 4.1.3) on void growth, paying specific attention to the evolution of the volume and the geometry of the void during loading. Note that, following Bryhni Dæhli et al. (2017a), we could have exploited the symmetry of the problem and performed the calculations modeling 1/8 of the unit-cell. However, we have considered the whole unit-cell in order to be consistent with the calculations performed in Section 4.2 in which the misalignment between the principal directions of stress and strain breaks the symmetry of the problem, preventing the use of a simplified geometric model. As mentioned before, all the results reported in this section correspond to aluminium alloy 2090-T3. The notation for the material orientations investigated in the calculations performed in this section is  $x^{\Sigma_{III}}y^{\Sigma_I}z^{\Sigma_{II}}$ ,  $y^{\Sigma_{III}}z^{\Sigma_I}x^{\Sigma_{II}}$  and  $z^{\Sigma_{III}}x^{\Sigma_I}y^{\Sigma_{II}}$ , where the first, second and third letters indicate the orthotropy axes corresponding to the minor, major and intermediate loading directions, respectively, see Fig. 3.

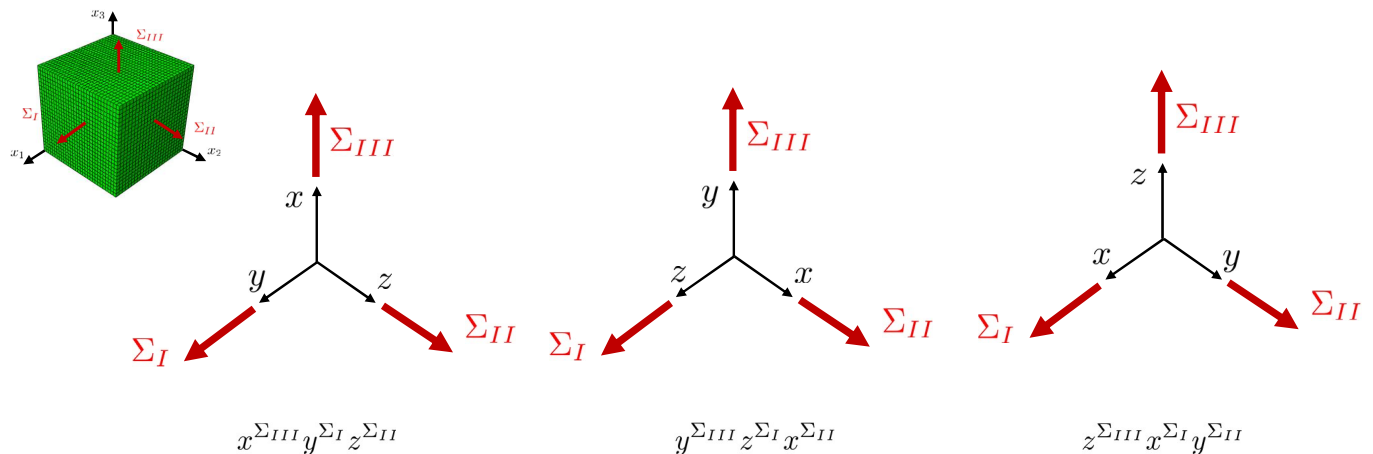


Figure 3: Schematic representation for the material orientations investigated in the calculations reported in this section,  $x^{\Sigma_{III}}y^{\Sigma_I}z^{\Sigma_{II}}$ ,  $y^{\Sigma_{III}}z^{\Sigma_I}x^{\Sigma_{II}}$  and  $z^{\Sigma_{III}}x^{\Sigma_I}y^{\Sigma_{II}}$ , where the first, second and third letters indicate the orthotropy axes corresponding to the minor, major and intermediate loading directions, respectively.

##### 4.1.1. The influence of stress triaxiality

Fig. 4 shows the evolution of the normalized void volume fraction  $f/f_0$  with the macroscopic effective strain  $\bar{\epsilon}$  for three values of the macroscopic stress triaxiality  $T = 0.33, 1$  and  $2$ . The Lode parameter is  $L = -1$  so that the loading

in directions  $x_2$  and  $x_3$  is the same. The void volume fraction,  $f$ , is calculated using the Quickhull algorithm (Barber et al., 1996) to compute the smallest convex set containing the coordinates of the nodes that form the surface of the void. The convex hull is determined at each time increment, thus obtaining the evolution of the void volume fraction during loading. Results are shown for the von Mises material, Fig. 4(a), and for the material modeled with Yld2004-18p yield criterion with orientation  $x^{\Sigma_{III}}y^{\Sigma_I}z^{\Sigma_{II}}$ , Fig. 4(b), so that the minor loading direction  $x_3$  is parallel to the rolling direction  $x$ . Recall from Section 2 that the results for the isotropic von Mises (1928) material are obtained imposing  $c'_{ij} = c''_{ij} = 1$  and  $a = 2$  in the Yld2004-18p criterion, see equations (6) and (8). For both yield functions the volume of the void increases with the effective strain and the triaxiality. Note that, while for  $T = 1$  and 2 the void volume fraction increases slightly faster for the von Mises material (check the intersection of the red and green dashed curves with the axis  $f/f_0 = 1.7$ ), for  $T = 0.33$  the increase of porosity is slightly greater for the Yld2004-18p criterion (check the intersection of the solid black curves with the axis  $\bar{\varepsilon} = 0.4$ ), bringing out that the quantitative effect of the triaxiality on void growth depends on the plastic anisotropy. Note that we have also checked that the rate of growth of the void depends on the material orientation, i.e., quantitative differences are obtained for the simulations performed with  $y^{\Sigma_{III}}z^{\Sigma_I}x^{\Sigma_{II}}$  and  $z^{\Sigma_{III}}x^{\Sigma_I}y^{\Sigma_{II}}$ . Nevertheless, these results are not shown here for the sake of brevity.

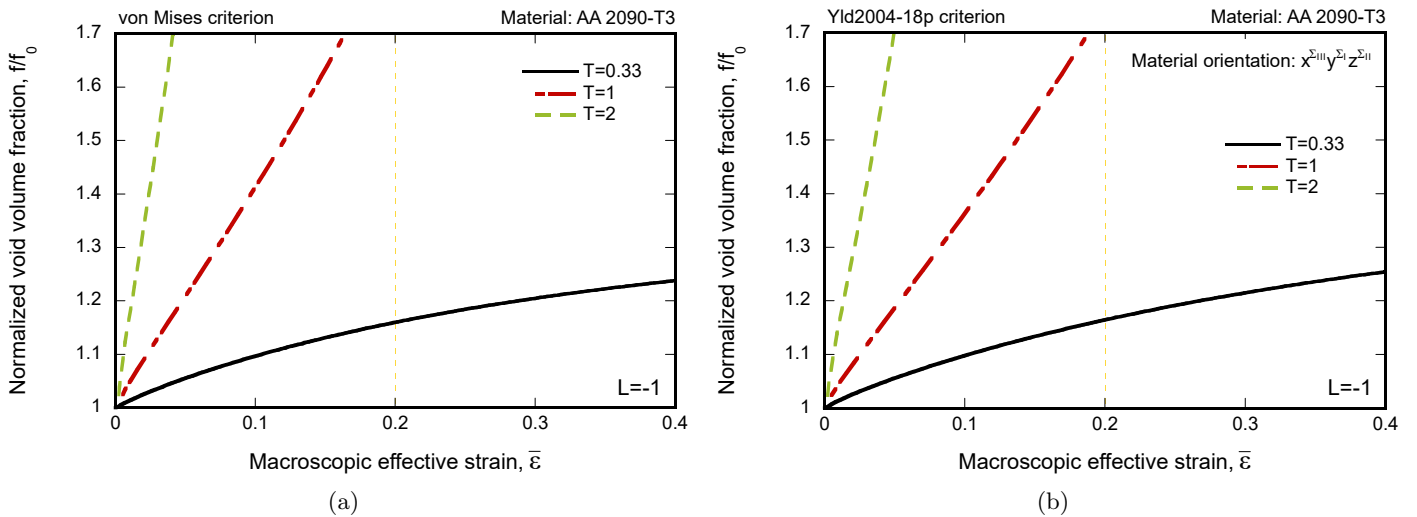


Figure 4: Influence of the macroscopic stress triaxiality on void growth for AA 2090-T3. Unit-cell finite element calculations for  $L = -1$  (axisymmetric tension) and three values of stress triaxiality  $T = 0.33, 1$  and  $2$ . Evolution of the normalized void volume fraction  $f/f_0$  with the macroscopic effective strain  $\bar{\varepsilon}$  for: (a) von Mises (1928) yield criterion and (b) Yld2004-18p yield criterion (Barlat et al., 2005) with material orientation  $x^{\Sigma_{III}}y^{\Sigma_I}z^{\Sigma_{II}}$ . The dashed yellow line corresponds to the macroscopic effective strain  $\bar{\varepsilon} = 0.2$ . (For interpretation of the references to color in this figure legend, the reader is referred to the web version of this article.)

The interplay between the shape of the void, the macroscopic triaxiality and the plastic anisotropy is illustrated in Fig. 5, which shows contours of effective plastic strain in the matrix material  $\bar{\varepsilon}_p$  for the same calculations presented in Fig. 4, and the loading time corresponding to the macroscopic effective strain  $\bar{\varepsilon} = 0.2$  (vertical yellow dashed line

in Fig. 4). The contour plots correspond to the cut-view  $x_2 = \frac{L_0}{2}$  (mid-plane of the unit-cell), and the color coding is such that effective plastic strains ranging from 0 to 0.4 correlate with a color scale that goes from blue to red. If the value of the effective plastic strain is above 0.4, it remains red. The contour plots show that the plastic strain fields are symmetric with respect to the loading axes and that the size of the plastically deformed zone is greater for the calculations performed with von Mises plasticity (check the extension of the red area). The shape of the void is ellipsoidal and approaches sphericity as the triaxiality increases for both constitutive models. However, while for the calculations performed with von Mises plasticity the void turns out to be a spheroid, for the anisotropic matrix the three semi-axes of the ellipsoid are different, as further illustrated in Fig. 6, which shows the evolution of the ratios  $\frac{b}{a}$  and  $\frac{c}{a}$  with the macroscopic effective strain  $\bar{\epsilon}$ , where  $a$ ,  $b$  and  $c$  refer to the semi-axes of the void parallel to the loading directions  $x_1$  (major loading direction),  $x_2$  and  $x_3$  (minor loading direction), respectively (notice in Fig. 2 that in the undeformed configuration,  $a$ ,  $b$  and  $c$  were denoted by  $a_0$ ,  $b_0$  and  $c_0$ , respectively). In the calculations performed with von Mises plasticity, Fig. 5(a), we have that  $\frac{b}{a} = \frac{c}{a}$  for the three triaxialities. For  $T = 0.33$  and 1, the ratios  $\frac{b}{a} = \frac{c}{a}$  decrease with the macroscopic effective strain due to the elongation of the void. In contrast, for  $T = 2$  the semi-axes relation is  $\approx 1$  until  $\bar{\epsilon} \approx 0.2$  (the void remains spherical during loading) and then increases, indicating that the void starts to grow faster in directions  $x_2$  and  $x_3$  than in the main loading direction. Moreover, Fig. 6(b) shows that in the calculations with Yld2004-18p criterion  $\frac{c}{a} > \frac{b}{a}$ , i.e., the void grows more in the rolling than in the normal direction of anisotropy (rolling and normal directions are parallel to  $x_3$  and  $x_2$ , respectively). This seems to be consistent with the results of Fig. 1(a) which showed that the material yields earlier in the rolling direction, favoring faster void expansion along  $x_3$ . Notice that the greatest difference between the ratios  $\frac{b}{a}$  and  $\frac{c}{a}$ , for the range of macroscopic effective strains shown in Fig. 6(b), corresponds to  $T = 2$ .

#### 4.1.2. The influence of Lode parameter

Fig. 7 illustrates the influence of the Lode parameter on the evolution of the normalized void volume fraction  $f/f_0$  with the macroscopic effective strain  $\bar{\epsilon}$ . Calculations are shown for  $L = -1, 0$  and 1, using von Mises and Yld2004-18p yield criteria, and for two different values of the macroscopic triaxiality  $T = 0.33$  and 1. Recall that  $L = -1, 0$  and 1 represent states of axisymmetric tension, generalized shear, and axisymmetric compression, respectively.

The results obtained for  $T = 0.33$  are included in Figs. 7(a) and 7(b). For the von Mises material, Fig. 7(a), the  $f/f_0 - \bar{\epsilon}$  curve is shifted upwards as the Lode parameter goes from 1 to  $-1$ , with the normalized void volume fraction for  $L = 0$  and  $L = 1$  displaying a maximum for an intermediate value of the macroscopic effective strain (the maximum of  $f/f_0$  for  $L = -1$  is attained for a larger strain  $\bar{\epsilon} > 0.6$ ). For the Yld2004-18p yield criterion, Fig. 7(b), the results correspond to the material orientation  $z^{\Sigma_{III}} x^{\Sigma_I} y^{\Sigma_{II}}$ , so that the minor loading direction  $x_3$  is collinear to the normal orthotropy axis  $z$ . As the loading process starts, the void grows faster for  $L = 1$  than for  $L = 0$  and  $-1$ , i.e., the effect

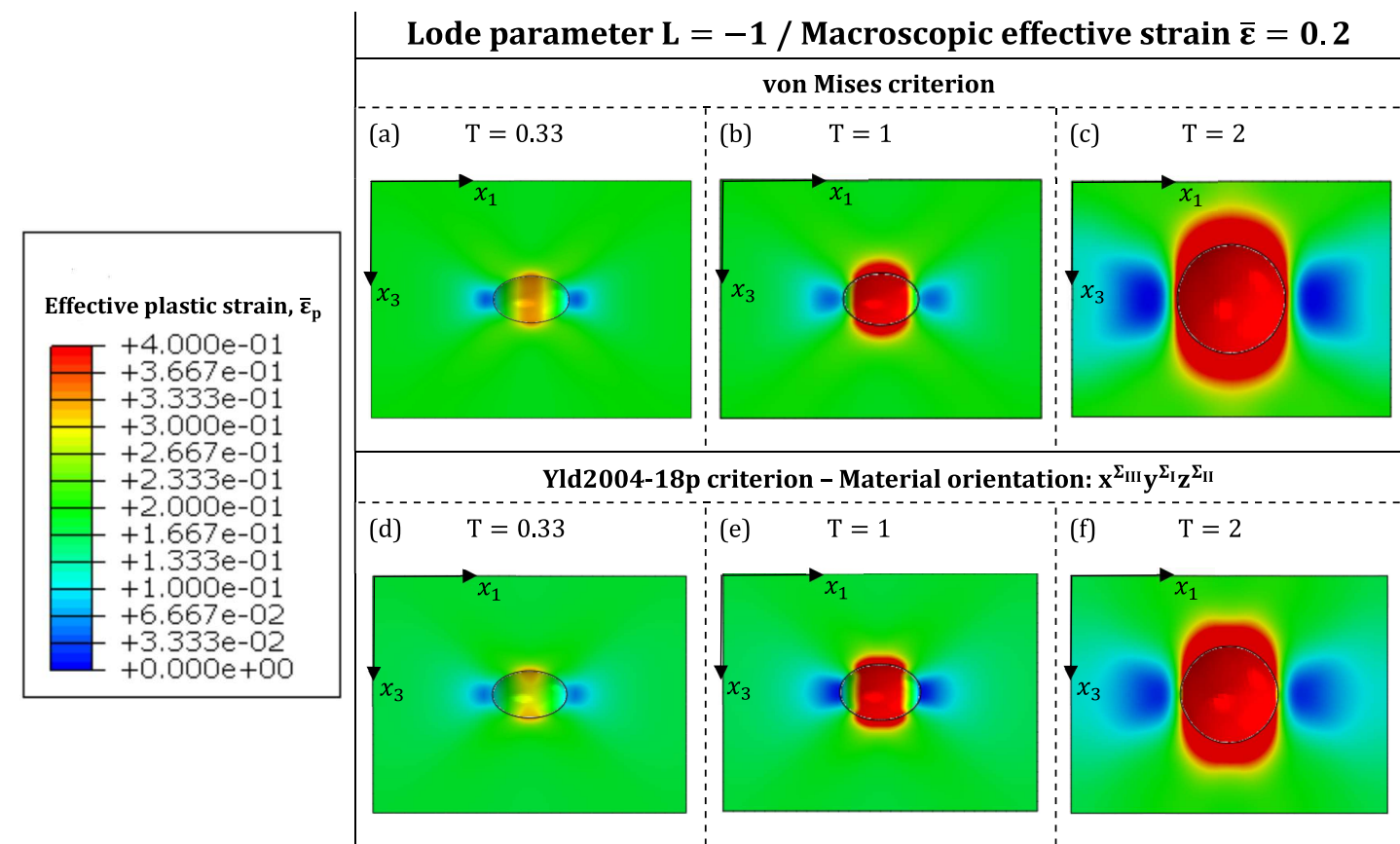


Figure 5: Influence of the macroscopic stress triaxiality on void growth for AA 2090-T3. Contours of effective plastic strain in the matrix material  $\bar{\epsilon}_p$  for unit-cell finite element calculations performed with Lode parameter  $L = -1$  (axisymmetric tension). Cut-view for  $x_2 = L_0/2$ . The macroscopic effective strain is  $\bar{\epsilon} = 0.2$ . Calculations performed with von Mises (1928) yield criterion and three values of stress triaxiality: (a)  $T = 0.33$ , (b)  $T = 1$  and (c)  $T = 2$ . Calculations performed with Yld2004-18p yield criterion (Barlat et al., 2005) with material orientation  $x^{\Sigma_{III}}y^{\Sigma_I}z^{\Sigma_{II}}$  and three values of stress triaxiality: (d)  $T = 0.33$ , (e)  $T = 1$  and (f)  $T = 2$ . (For interpretation of the references to color in this figure legend, the reader is referred to the web version of this article.)

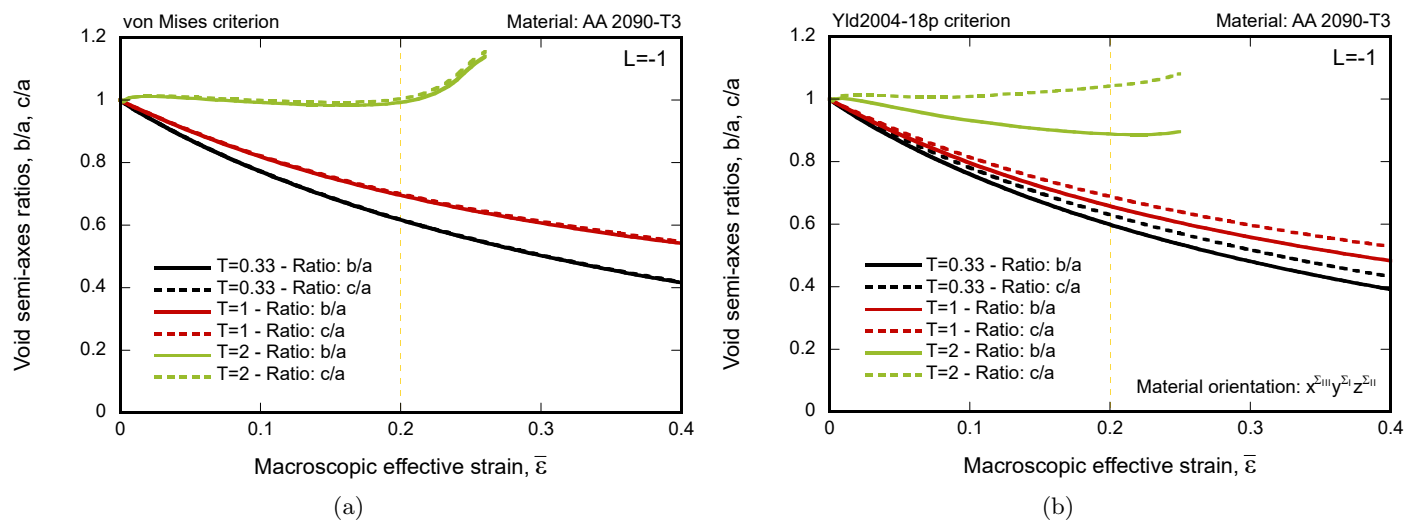


Figure 6: Influence of the macroscopic stress triaxiality on void growth for AA 2090-T3. Unit-cell finite element calculations with Lode parameter  $L = -1$  (axisymmetric tension) and three values of stress triaxiality  $T = 0.33, 1$  and  $2$ . Evolution of the void semi-axes ratios,  $b/a$  and  $c/a$ , with the macroscopic effective strain  $\bar{\epsilon}$  for: (a) von Mises (1928) yield criterion and (b) Yld2004-18p yield criterion (Barlat et al., 2005) with material orientation  $x^{\Sigma_{III}}y^{\Sigma_I}z^{\Sigma_{II}}$ . The dashed yellow line corresponds to the macroscopic effective strain  $\bar{\epsilon} = 0.2$ . (For interpretation of the references to color in this figure legend, the reader is referred to the web version of this article.)

of the Lode parameter on the relative order of the  $f/f_0 - \bar{\epsilon}$  curves is different than for the von Mises material. These results bring out that the effect of Lode parameter on void growth depends on the material anisotropy. Nevertheless, this change in the effect of the Lode parameter is specific of the  $z^{\Sigma_{III}}x^{\Sigma_I}y^{\Sigma_{II}}$  orientation, since for  $x^{\Sigma_{III}}y^{\Sigma_I}z^{\Sigma_{II}}$  and  $y^{\Sigma_{III}}z^{\Sigma_I}x^{\Sigma_{II}}$  the arrangement of the  $f/f_0 - \bar{\epsilon}$  curves is the same obtained for the von Mises material (these results are not shown here for the sake of brevity).

Figs. 7(c) and 7(d) display the results for  $T = 1$ . For the von Mises material, Fig. 7(c), the  $f/f_0 - \bar{\epsilon}$  curve is shifted downwards as the  $L$  goes from  $-1$  to  $1$ , with small differences between the results obtained with different values of the Lode parameter. Nevertheless, the Lode parameter affects the geometry of the void, that turns from a spheroid elongated along the  $x_1$  direction for  $L = -1$  to a penny shape spheroid flattened along the  $x_3$  direction for  $L = 1$ , as illustrated in the 3D reconstructions of the voids shown in Figs. 8(a) and 8(b). The void geometry is reconstructed plotting the surface defined by the convex hull that forms the surface of the void. The initial diameter of the void is 1. Specifically, Fig. 9(a) shows that for the von Mises yield criterion with  $L = -1$  the ratios of the ellipsoid semi-axes are  $\frac{b}{a} = \frac{c}{a}$ , while for  $L = 1$  the ratio  $\frac{c}{a}$  decreases with the macroscopic effective strain and  $\frac{b}{a} = 1$ , indicating that the void grows the same in directions  $x_1$  (major loading direction) and  $x_2$  (because  $L = 1$  corresponds to axisymmetric compression). Similar results were reported for von Mises materials by Cao et al. (2015) among others. For the anisotropic material, Fig. 7(d), the orientation of the uni-cell is  $y^{\Sigma_{III}}z^{\Sigma_I}x^{\Sigma_{II}}$ , so that the minor loading direction  $x_3$  is parallel to the transverse orthotropy axis  $y$ . The arrangement of the  $f/f_0 - \bar{\epsilon}$  curves is such that, as opposed to the isotropic case, the results for  $L = 1$  lie slightly above the results for  $L = 0$ . In addition, the void grows significantly faster for the Lode parameter  $L = -1$ , as it is apparent from the 3D reconstructions of the voids shown in Figs. 8(c) and 8(d) which illustrate that, for a fixed macroscopic strain  $\bar{\epsilon} = 0.2$ , the volume of the void is greater for  $L = -1$  than for  $L = 1$ . It is evident that the Lode parameter influences the shape of the void in the calculations performed with the anisotropic material differently than it does for the von Mises material. Specifically, Fig. 9(b) shows that for the anisotropic material and  $L = -1$  the void is no longer a spheroid since  $\frac{b}{a} \neq \frac{c}{a}$ , and for  $L = 1$  the elongation of the void in directions  $x_1$  and  $x_2$  is different, so that  $\frac{b}{a} \neq 1$ .

#### 4.1.3. The influence of material orientation

Fig. 10 pictures the normalized void volume fraction  $f/f_0$  versus the macroscopic effective strain  $\bar{\epsilon}$  for macroscopic stress triaxiality  $T = 2$  and two different values of the Lode parameter,  $L = 0$  and  $L = 1$ . Results corresponding to von Mises plasticity are compared with calculations performed with Yld2004-18p criterion for three material orientations  $x^{\Sigma_{III}}y^{\Sigma_I}z^{\Sigma_{II}}$ ,  $y^{\Sigma_{III}}z^{\Sigma_I}x^{\Sigma_{II}}$  and  $z^{\Sigma_{III}}x^{\Sigma_I}y^{\Sigma_{II}}$  (i.e., the minor loading direction is collinear to the rolling, the transverse and the normal orthotropy axis, respectively).

The calculations corresponding to the Lode parameter  $L = 0$  are shown in Fig. 10(a). The relative order of the

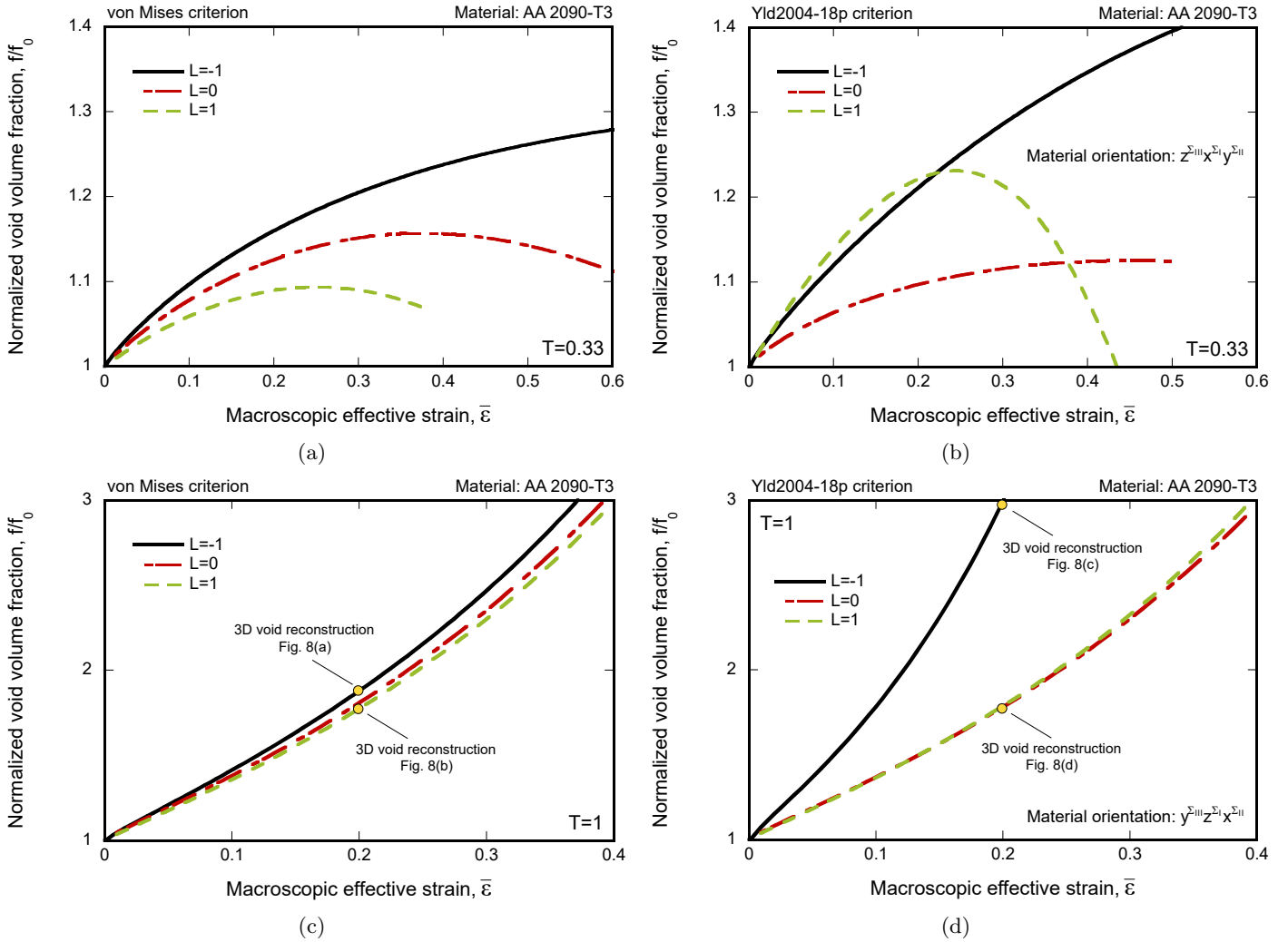


Figure 7: Influence of the macroscopic Lode parameter on void growth for AA 2090-T3. Unit-cell finite element calculations for three different values of the Lode parameter  $L = -1, 0$  and  $1$  (axisymmetric tension, generalized shear and axisymmetric compression). Evolution of the normalized void volume fraction  $f/f_0$  with the macroscopic effective strain  $\bar{\epsilon}$ . Macroscopic stress triaxiality  $T = 0.33$ : (a) von Mises (1928) yield criterion and (b) Yld2004-18p yield criterion (Barlat et al., 2005) with material orientation  $z^{\Sigma_{III}} x^{\Sigma_I} y^{\Sigma_{II}}$ . Macroscopic stress triaxiality  $T = 1$ : (c) von Mises yield criterion and (d) Yld2004-18p yield criterion (Barlat et al., 2005) with material orientation  $y^{\Sigma_{III}} z^{\Sigma_I} x^{\Sigma_{II}}$ .

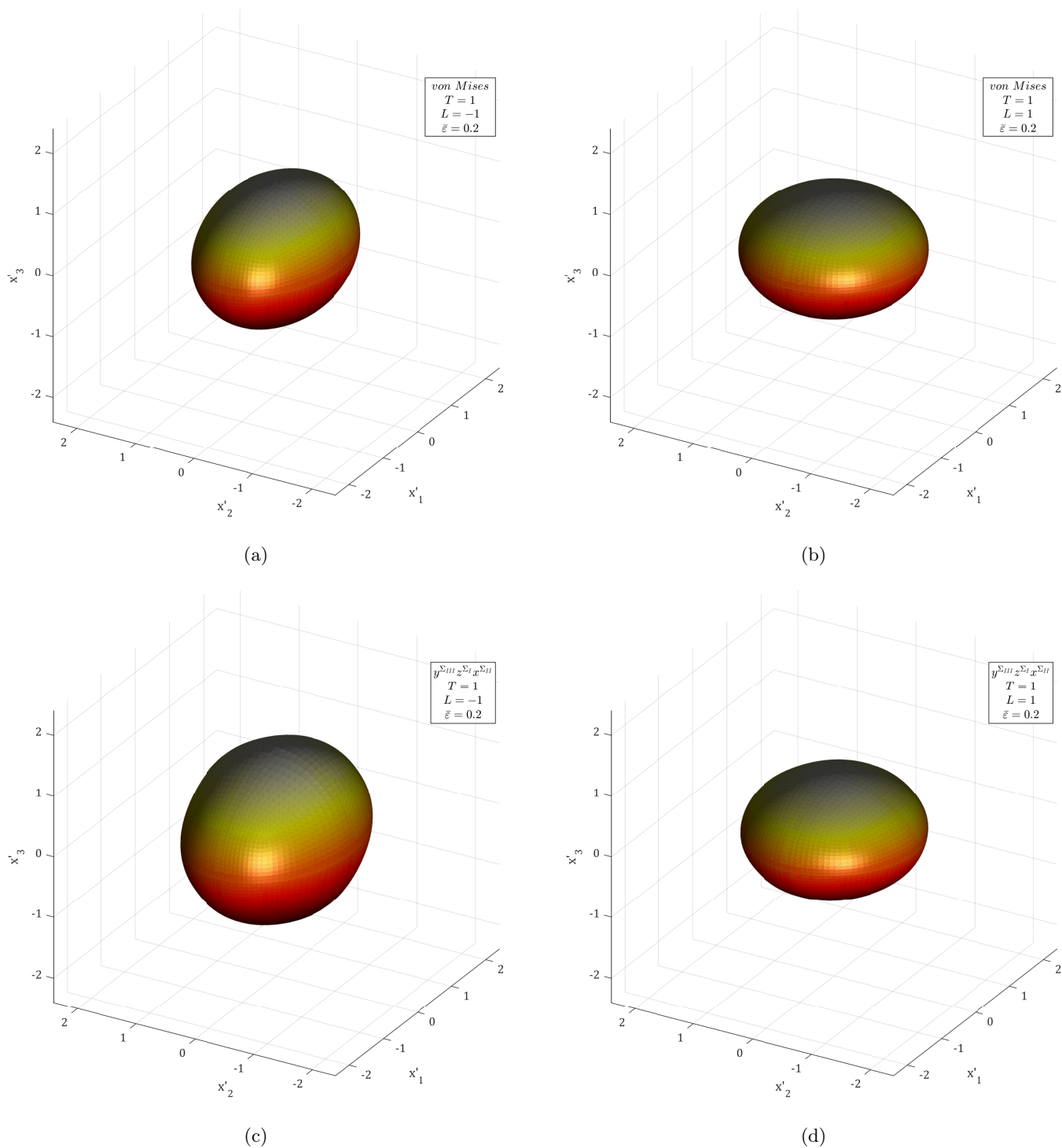


Figure 8: 3D reconstruction of the surface of the voids for AA 2090-T3. The macroscopic stress triaxiality and the effective strain are  $T = 1$  and  $\bar{\varepsilon} = 0.2$ , respectively. Results for von Mises (1928) yield criterion: (a)  $L = -1$  (axisymmetric tension) and (c)  $L = 1$  (axisymmetric compression). Results for Yld2004-18p yield criterion (Barlat et al., 2005) with material orientation  $y^{\Sigma III} z^{\Sigma I} x^{\Sigma II}$ : (c)  $L = -1$  (axisymmetric tension) and (d)  $L = 1$  (axisymmetric compression). The origin of the Cartesian coordinate system ( $x'_1, x'_2, x'_3$ ) is located at the center of mass of the void, with  $x'_1, x'_2$  and  $x'_3$  being parallel to the loading axes  $x_1, x_2$  and  $x_3$ . The initial diameter of the void is 1.

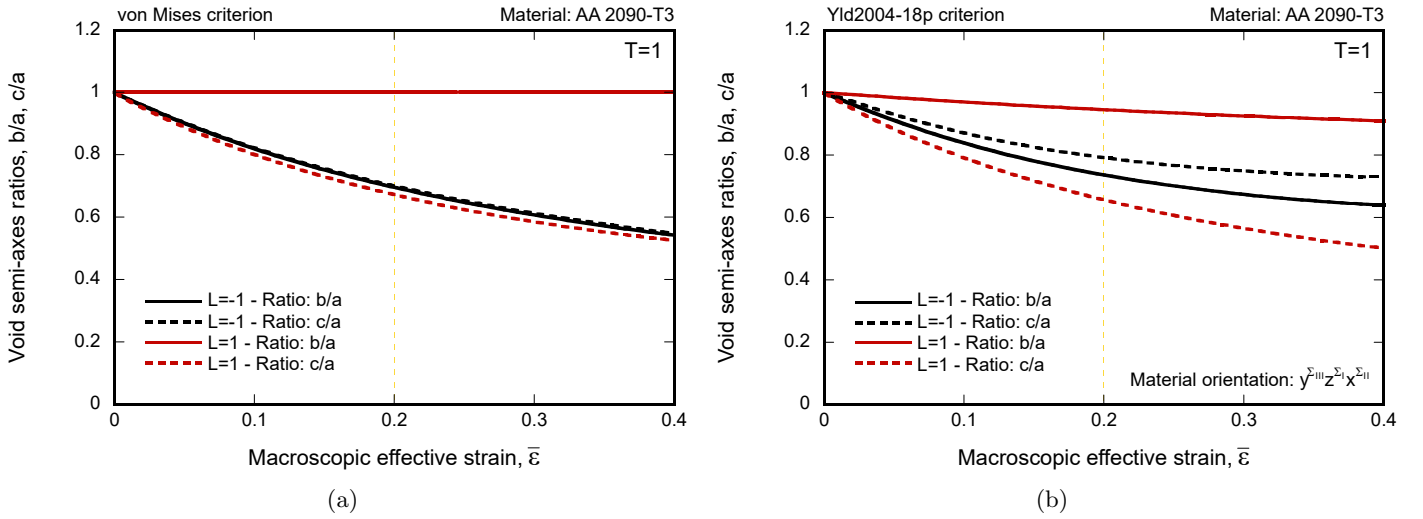


Figure 9: Influence of the macroscopic Lode parameter on void growth for AA 2090-T3. Unit-cell finite element calculations for  $T = 1$  and two different values of the macroscopic Lode parameter  $L = -1$  and  $1$  (axisymmetric tension and axisymmetric compression, respectively). Evolution of the void semi-axes ratios,  $b/a$  and  $c/a$ , with the macroscopic effective strain  $\bar{\epsilon}$  for: (a) von Mises (1928) yield criterion and (b) Yld2004-18p yield criterion (Barlat et al., 2005) with material orientation  $y^{\Sigma_{III}} z^{\Sigma_I} x^{\Sigma_{II}}$ . The dashed yellow line corresponds to the macroscopic effective strain  $\bar{\epsilon} = 0.2$ . (For interpretation of the references to color in this figure legend, the reader is referred to the web version of this article.)

406  $f/f_0 - \bar{\epsilon}$  curves obtained with the anisotropic model is such that the porosity grows faster for the orientation  $x^{\Sigma_{III}} y^{\Sigma_I} z^{\Sigma_{II}}$ ,  
 407 whereas the curves for  $y^{\Sigma_{III}} z^{\Sigma_I} x^{\Sigma_{II}}$  and  $z^{\Sigma_{III}} x^{\Sigma_I} y^{\Sigma_{II}}$  virtually overlap each other for most of the range of macroscopic  
 408 strains considered in the plot. On the other hand, the  $f/f_0 - \bar{\epsilon}$  curve obtained with the von Mises yield criterion lies  
 409 between the results corresponding to  $x^{\Sigma_{III}} y^{\Sigma_I} z^{\Sigma_{II}}$  and the other two material orientations. The geometry of the voids for  
 410 a fixed value of the macroscopic strain  $\bar{\epsilon} = 0.15$  is shown in Fig. 11. While the shape of the void for von Mises plasticity,  
 411 Fig. 11(a), is roughly spherical with  $\frac{b}{a} \approx 1.01$  and  $\frac{c}{a} \approx 0.92$ , the anisotropy leads to important variations in the void  
 412 geometry, which is shown to be dependent on the material orientation. Specifically, for the orientation  $x^{\Sigma_{III}} y^{\Sigma_I} z^{\Sigma_{II}}$  the  
 413 semi-axes aspect ratios are  $\frac{c}{a} \approx 1.06$  and  $\frac{b}{a} \approx 0.93$ , so that the void grows more rapidly in the  $x_3$  direction than in the  
 414 major loading direction (which corresponds to  $x_1$ ). In contrast, for the orientations  $y^{\Sigma_{III}} z^{\Sigma_I} x^{\Sigma_{II}}$  and  $z^{\Sigma_{III}} x^{\Sigma_I} y^{\Sigma_{II}}$ , we  
 415 have that  $\frac{c}{a} < 1$  and  $\frac{b}{a} > 1$ , so that the voids are stretched out along direction  $x_2$ . Specifically, for the case  $y^{\Sigma_{III}} z^{\Sigma_I} x^{\Sigma_{II}}$   
 416 we have that  $\frac{c}{a} \approx 0.88$  and  $\frac{b}{a} \approx 1.06$ , and for the orientation  $z^{\Sigma_{III}} x^{\Sigma_I} y^{\Sigma_{II}}$  the ratios are  $\frac{c}{a} \approx 0.96$  and  $\frac{b}{a} \approx 1.06$ ,  
 417 i.e., in the latter case the void is comparatively more elongated along the  $x_3$  direction. The finite element simulations  
 418 performed for  $L = 1$  are reported in Fig. 10(b). The arrangement of the  $f/f_0 - \bar{\epsilon}$  curves is different than in the case  
 419 of  $L = 0$ , and the fastest growth rate is obtained for the anisotropic material with  $z^{\Sigma_{III}} x^{\Sigma_I} y^{\Sigma_{II}}$  orientation, followed  
 420 by the orientation  $x^{\Sigma_{III}} y^{\Sigma_I} z^{\Sigma_{II}}$ , the von Mises material and the anisotropic material with orientation  $y^{\Sigma_{III}} z^{\Sigma_I} x^{\Sigma_{II}}$ ,  
 421 respectively. In agreement with the conclusions derived from the analysis of Bryhni Dæhli et al. (2017a) for different  
 422 textured face-centered-cubic metals, these numerical results demonstrate that the anisotropy of the matrix has a marked  
 423 effect on the growth and geometry evolution of the void.

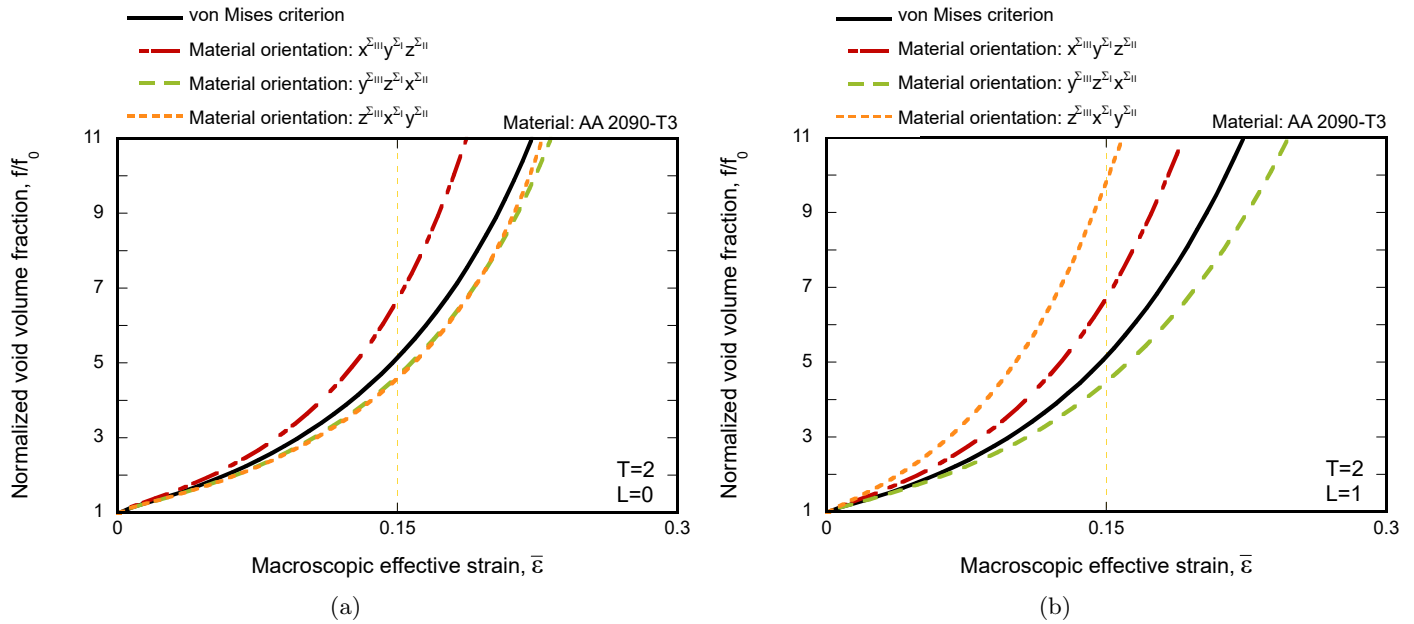


Figure 10: Influence of the material orientation on void growth for AA 2090-T3. Unit-cell finite element calculations for von Mises (1928) criterion and Yld2004-18p criterion (Barlat et al., 2005) with three material orientations  $x^{\Sigma_{III}}y^{\Sigma_I}z^{\Sigma_{II}}$ ,  $y^{\Sigma_{III}}z^{\Sigma_I}x^{\Sigma_{II}}$  and  $z^{\Sigma_{III}}x^{\Sigma_I}y^{\Sigma_{II}}$ . Evolution of the normalized void volume fraction  $f/f_0$  with the macroscopic effective strain  $\bar{\epsilon}$ . Macroscopic stress triaxiality  $T = 2$  and Lode parameter: (a)  $L = 0$  (generalized shear) and (b)  $L = 1$  (axisymmetric compression). The dashed yellow line corresponds to the macroscopic effective strain  $\bar{\epsilon} = 0.15$ . (For interpretation of the references to color in this figure legend, the reader is referred to the web version of this article.)

Moreover, note that we have not observed the void to coalesce for the range of macroscopic effective strains and void volume fractions considered in these calculations. Recall that the main objective of the paper is to identify the role of anisotropy and material orientation on void growth, so that the analysis is limited to *moderate* levels of  $\bar{\epsilon}$  and  $f/f_0$ . However, we have checked that for greater macroscopic effective strains, and larger void volume fraction, coalescence may occur, and for some loading cases and material orientations, a pair of localization bands is formed inside the inter-void ligament. Nevertheless, large void growth is accompanied by important mesh distortion, so that alternative procedures, e.g. Eulerian analysis, are needed to provide a complete description of localization and failure.

#### 4.2. Misalignment between loading and material axes

Following the same scheme of Section 4.1, we carry out a parametric study on the influence of macroscopic stress triaxiality (Section 4.2.1), Lode parameter (Section 4.2.2) and material orientation (Section 4.2.3) on the evolution of the size and the shape of the void. Recall that in the calculations in which loading and material axes are not parallel, the material orthotropy axes rotate relative to the loading directions during loading. We investigate angular misalignments within the range  $0^\circ \leq \theta \leq 90^\circ$  –calculations performed in eight intervals of  $11.25^\circ$ –, so that one loading direction is collinear to one of the symmetry axes of the material, and  $\theta$  is the angle formed between the other two loading directions and the second and third orthotropy axes. The notation for the material orientations investigated

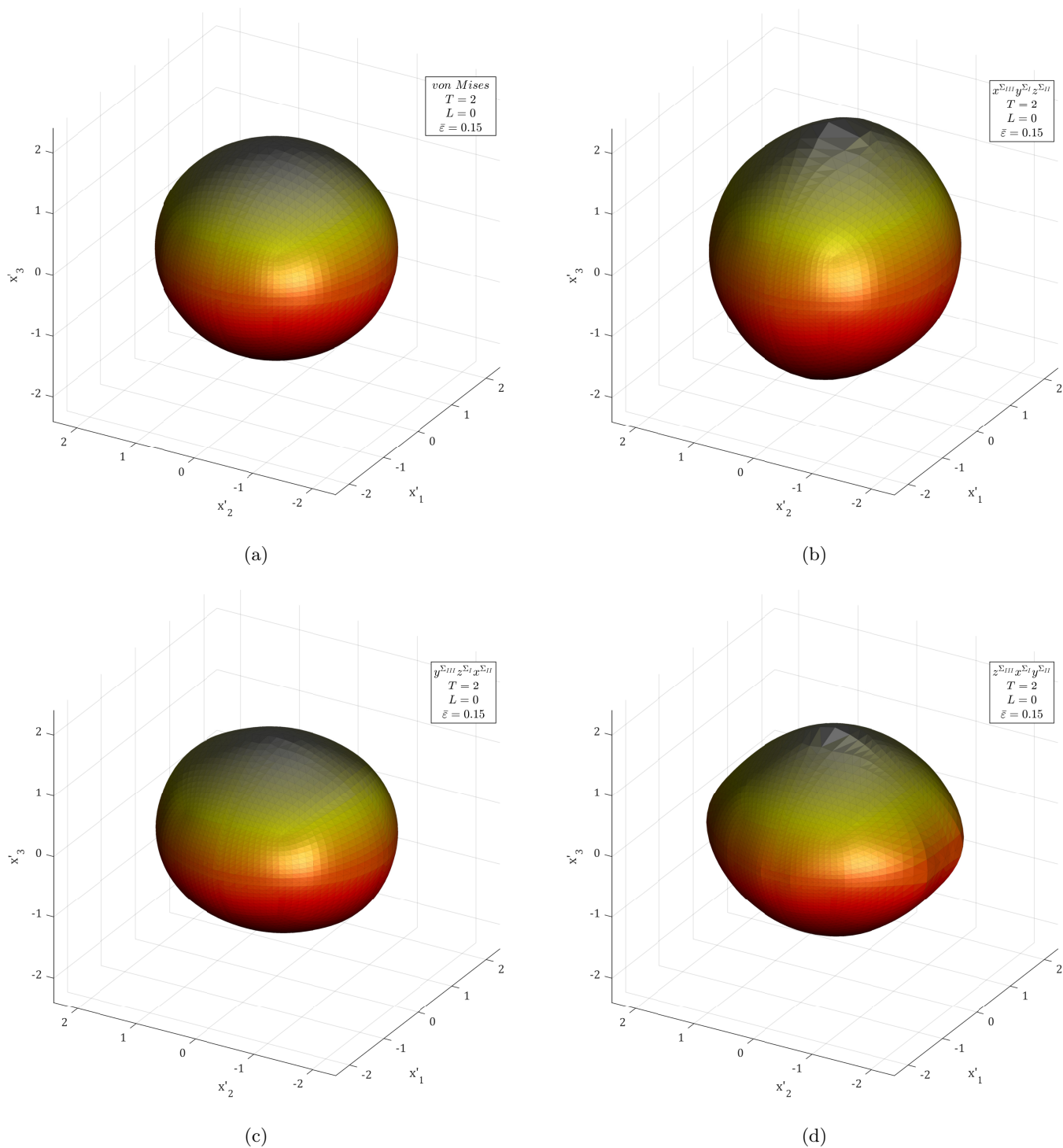


Figure 11: 3D reconstruction of the surface of the voids for AA 2090-T3. The macroscopic stress triaxiality, the macroscopic Lode parameter and the macroscopic effective strain are  $T = 2$ ,  $L = 0$  (generalized shear), and  $\bar{\varepsilon} = 0.15$ , respectively. Results for: (a) von Mises (1928) yield criterion and Yld2004-18p yield criterion (Barlat et al., 2005) for (b)  $x^{\Sigma_{III}} y^{\Sigma_{I}} z^{\Sigma_{III}}$ , (c)  $y^{\Sigma_{III}} z^{\Sigma_{I}} x^{\Sigma_{III}}$  and (d)  $z^{\Sigma_{III}} x^{\Sigma_{I}} y^{\Sigma_{III}}$  orientations. The origin of the Cartesian coordinate system  $(x'_1, x'_2, x'_3)$  is located at the center of mass of the void, with  $x'_1$ ,  $x'_2$  and  $x'_3$  being parallel to the loading axes  $x_1$ ,  $x_2$  and  $x_3$ . The initial diameter of the void is 1.

440 in the calculations performed in this section is  $x^{\Sigma_{III}} y^{\theta} z^{\theta}$ ,  $y^{\Sigma_{III}} z^{\theta} x^{\theta}$  and  $z^{\Sigma_{III}} x^{\theta} y^{\theta}$ , where the first letter indicates the  
 441 orthotropy axis corresponding to the minor loading direction, and  $\theta$  is the angle formed between the other two loading

directions and orthotropy axes. An schematic representation for the specific orientations  $x^{\Sigma_{III}}y^{22.5^\circ}z^{22.5^\circ}$ ,  $x^{\Sigma_{III}}y^{45^\circ}z^{45^\circ}$  and  $x^{\Sigma_{III}}y^{67.5^\circ}z^{67.5^\circ}$ , where  $\theta = 22.5^\circ$ ,  $45^\circ$  and  $67.5^\circ$ , respectively, is shown in Fig. 12. We also perform calculations for material orientations  $x^{\Sigma_I}y^\theta z^\theta$ ,  $y^{\Sigma_I}z^\theta x^\theta$  and  $z^{\Sigma_I}x^\theta y^\theta$ , so that the first letter indicates the orthotropy axis corresponding to the major loading direction (see Fig. 26). Despite the misalignment between loading and orthotropy axes, which promotes the development of shear stresses near the void, macroscopic triaxiality and Lode parameter –prescribed using the multi-point constraint subroutine developed by Dakshinamurthy et al. (2021)– do not deviate more than 3% from the prescribed values during the entire loading process, for the range of macroscopic effective strains considered, and for all the calculations shown in this section. Note that the symmetry of the material with respect to the orthotropy axes makes the response of the cell the same for  $\pm\theta$ . Note also that due to the misalignment between loading and material axes, the faces of the unit-cell twist during loading, see Fig. 24, so that it is essential the application of periodic boundary conditions to the finite element model to allow the unit-cell to deform freely without constraints, see Section 3 and Dakshinamurthy et al. (2021). In addition, note that the deformed voids are not ellipsoidal (recall that the deformed voids in the calculations shown in Section 3 were ellipsoidal). In this section, results are presented for three aluminum alloys: 2090-T3, 6111-T4 and 6013. While a large number of works has been published so far to study void growth using unit-cell calculations, to the authors' knowledge, this is the first paper which includes simulations for anisotropic materials modeled with a macroscopic anisotropic yield function in which loading and materials axes are not aligned.

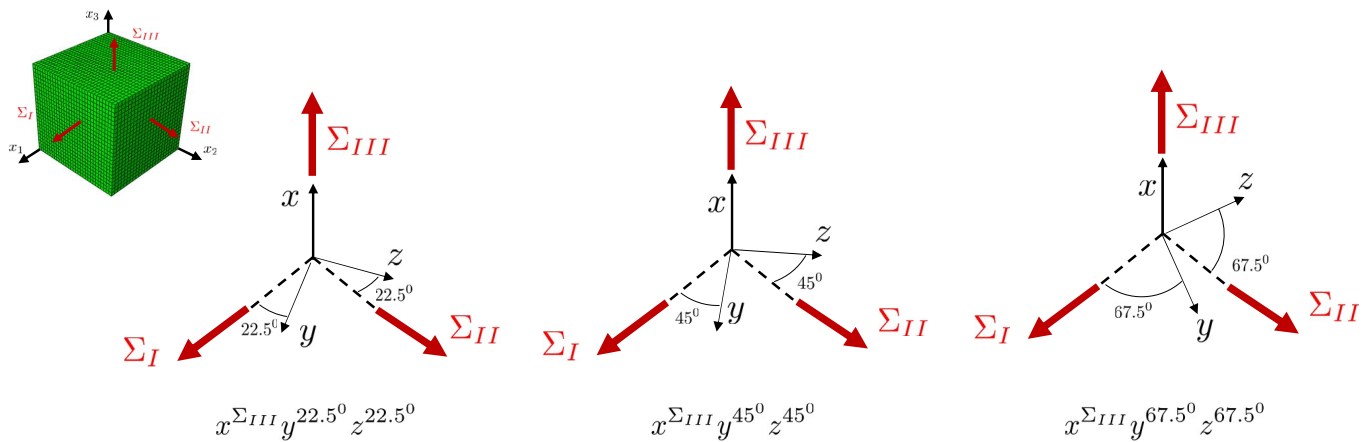


Figure 12: Schematic representation of material orientations investigated in the calculations reported in this section,  $x^{\Sigma_{III}}y^{22.5^\circ}z^{22.5^\circ}$ ,  $x^{\Sigma_{III}}y^{45^\circ}z^{45^\circ}$  and  $x^{\Sigma_{III}}y^{67.5^\circ}z^{67.5^\circ}$ , so that the minor loading direction  $x_3$  is parallel to the rolling direction  $x$ , and the transverse and normal orthotropy axes,  $y$  and  $z$ , form  $22.5^\circ$ ,  $45^\circ$  and  $67.5^\circ$ , respectively, with the other two loading directions.

#### 4.2.1. The influence of stress triaxiality

Fig. 13 shows the evolution of the normalized void volume fraction  $f/f_0$  with the macroscopic effective strain  $\bar{\epsilon}$  for  $L = -1$  and three different values of the stress triaxiality  $T = 0.33$ , 1 and 2. Results correspond to Yld2004-18p criterion and aluminium alloy 2090-T3 for three different material orientations,  $x^{\Sigma_{III}}y^{22.5^\circ}z^{22.5^\circ}$ ,  $x^{\Sigma_{III}}y^{45^\circ}z^{45^\circ}$  and

$x^{\Sigma_{III}} y^{67.5^\circ} z^{67.5^\circ}$ , so that the minor loading direction  $x_3$  is parallel to the rolling direction  $x$ , and the transverse and normal orthotropy axes,  $y$  and  $z$ , form  $22.5^\circ$ ,  $45^\circ$  and  $67.5^\circ$ , respectively, with the other two loading directions. The increase of triaxiality boosts the porosity growth for the three values of  $\theta$  considered, with the  $f/f_0 - \bar{\epsilon}$  curves obtained for  $T = 0.33$  displaying a concave-downwards shape, and the curves for  $T = 1$  and  $T = 2$  a concave-upwards shape, just like in the calculations shown in Section 4.1, in which loading directions and material axes were parallel. On the other hand, there is an important effect of the angular misalignment  $\theta$  on the void volume fraction so that the void grows faster for  $67.5^\circ$  than for  $45^\circ$  and  $22.5^\circ$ , for the three values of macroscopic triaxiality considered. The differences in the size and shape of the void with the angle  $\theta$  become apparent in Fig. 14 which pictures 3D reconstructions of the voids corresponding to the three orientations,  $x^{\Sigma_{III}} y^{22.5^\circ} z^{22.5^\circ}$ ,  $x^{\Sigma_{III}} y^{45^\circ} z^{45^\circ}$  and  $x^{\Sigma_{III}} y^{67.5^\circ} z^{67.5^\circ}$ , for  $T = 2$  and macroscopic effective strain  $\bar{\epsilon} = 0.15$  (yellow markers in the green dashed curves of Figs. 13(a), 13(b) and 13(c)). The void for  $x^{\Sigma_{III}} y^{67.5^\circ} z^{67.5^\circ}$  is bigger, and it is more elongated along the  $x_2$  direction, notably in comparison with the void corresponding to  $x^{\Sigma_{III}} y^{22.5^\circ} z^{22.5^\circ}$ , which is flattened along the second loading axis. Notice that, as mentioned before, the voids are not ellipsoidal. Nevertheless, unlike what it could be deduced from the results presented in Figs. 13 and 14, the relationship between void volume fraction and angular misalignment is strongly nonlinear ( $f/f_0$  is not an increasing function of  $\theta$ ), and it depends on the material orientation.

Fig. 15 shows the evolution of  $f/f_0$  with the angular misalignment  $\theta$  for the same macroscopic Lode parameter and the same values of the stress triaxiality considered in Fig. 13, and different material orientations:  $x^{\Sigma_{III}} y^\theta z^\theta$  (as in Fig. 13),  $y^{\Sigma_{III}} z^\theta x^\theta$  and  $z^{\Sigma_{III}} x^\theta y^\theta$ . Recall that the notation is such that in the case of  $x^{\Sigma_{III}} y^\theta z^\theta$  the minor loading direction  $x_3$  is parallel to the rolling direction  $x$ , and the transverse and normal orthotropy axes,  $y$  and  $z$ , form an angle  $\theta$  with the other two loading directions. The same reasoning is applied for  $y^{\Sigma_{III}} z^\theta x^\theta$  and  $z^{\Sigma_{III}} x^\theta y^\theta$ , for which the minor loading direction  $x_3$  is parallel to the orthotropy axes  $y$  and  $z$ , respectively. Notice that the void volume fraction, for the three material orientations, and the three values of triaxiality considered, first decreases with the angle  $\theta$ , reaches a minimum, and then increases. The minimum is shallow for  $T = 0.33$ , and much stronger for  $T = 2$ , so that the nonlinearity of the  $f/f_0 - \theta$  curves becomes more important as the triaxiality increases, bringing out the interplay between angular misalignment and stress triaxiality on void growth. To the authors' knowledge, this is an original outcome of this paper. The angle  $\theta$  for which the minimum occurs, while hardly dependent on the value of  $T$ , depends on the material orientation. Specifically, the results pictured in Fig. 15(a) show that for the orientation  $x^{\Sigma_{III}} y^\theta z^\theta$  the minimum occurs at  $\theta \approx 25^\circ$ , while in the cases of  $y^{\Sigma_{III}} z^\theta x^\theta$  and  $z^{\Sigma_{III}} x^\theta y^\theta$  shown in Figs. 15(b) and 15(c), the minimum occurs for greater angular misalignment, namely  $\theta \approx 45^\circ$  and  $\approx 50^\circ$ , respectively. Moreover, notice that the slope of the  $f/f_0 - \theta$  curves also depends on the material orientation. For example, the greatest decrease of  $f/f_0$  for small angular

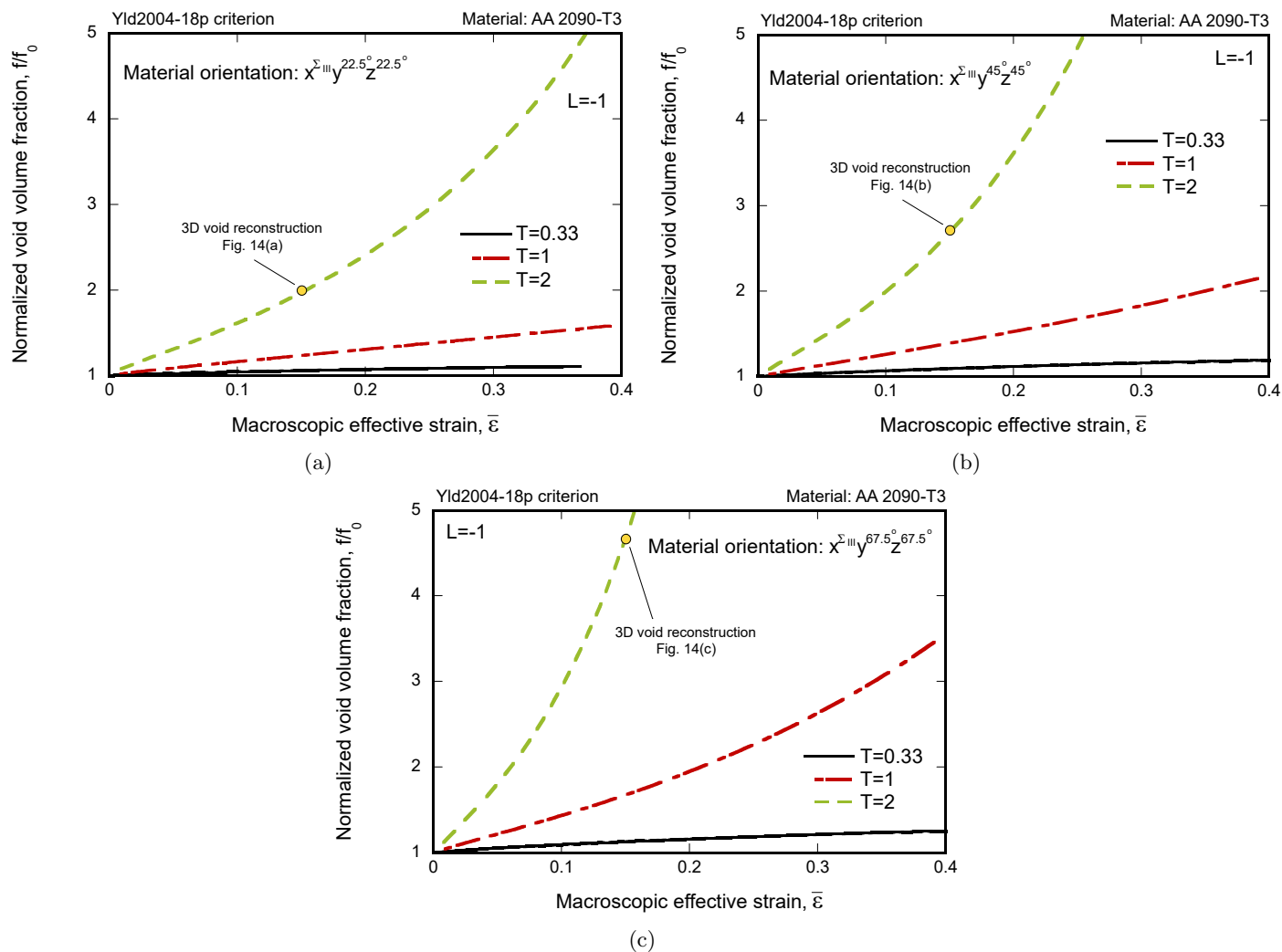


Figure 13: Influence of the macroscopic stress triaxiality on void growth for AA 2090-T3. Unit-cell finite element calculations for  $L = -1$  (axisymmetric tension) and three values of the stress triaxiality  $T = 0.33, 1$  and  $2$ . Evolution of the normalized void volume fraction  $f/f_0$  with the macroscopic effective strain  $\bar{\epsilon}$  for Yld2004-18p criterion (Barlat et al., 2005) with material orientation: (a)  $x^{\Sigma} y^{22.5^{\circ}} z^{22.5^{\circ}}$ , (b)  $x^{\Sigma} y^{45^{\circ}} z^{45^{\circ}}$  and (c)  $x^{\Sigma} y^{67.5^{\circ}} z^{67.5^{\circ}}$ . (For interpretation of the references to color in this figure legend, the reader is referred to the web version of this article.)

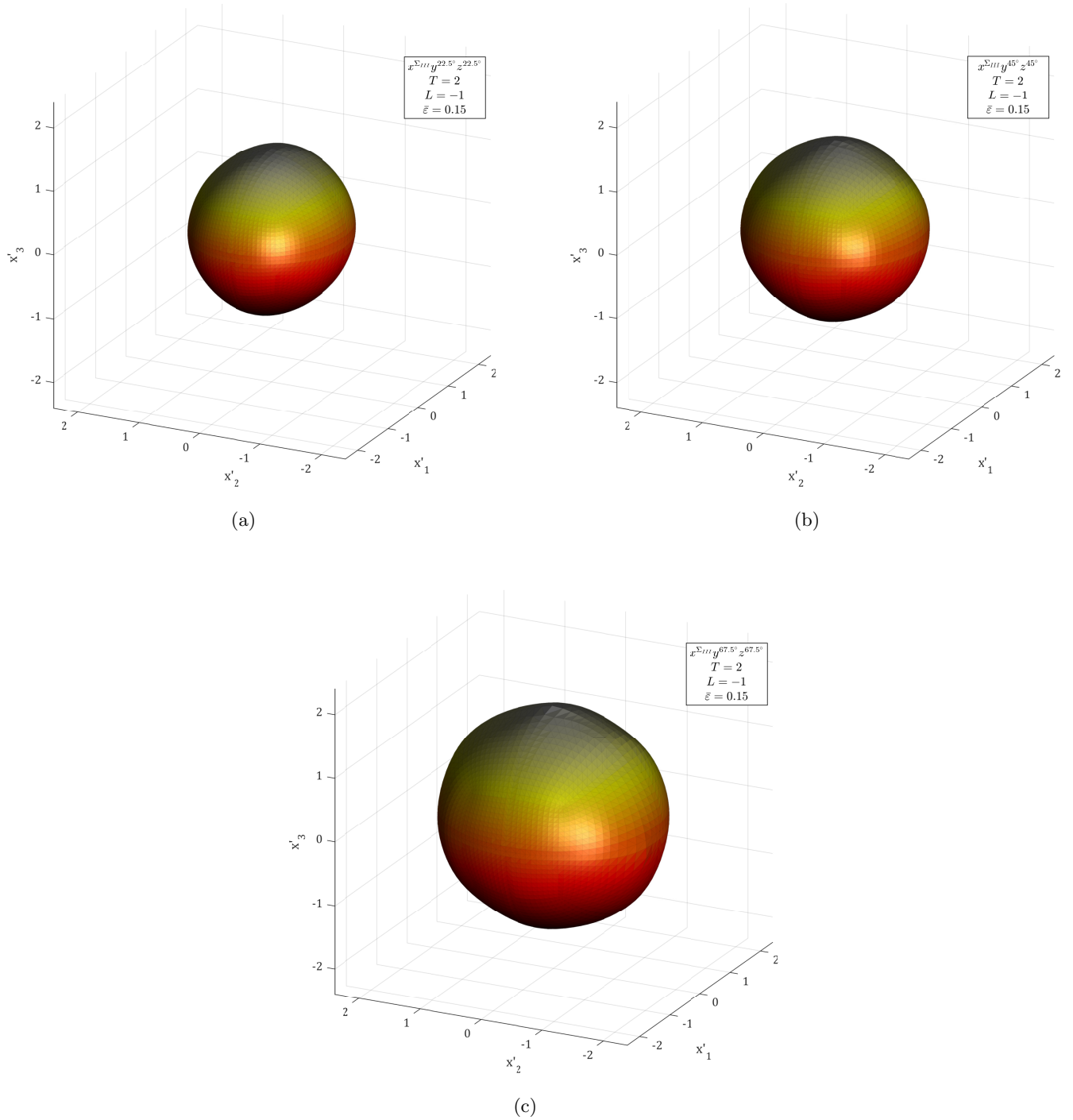


Figure 14: 3D reconstruction of the surface of the voids for AA 2090-T3. The Lode parameter is  $L = -1$  (axisymmetric tension) and the macroscopic triaxiality is  $T = 2$ . Results correspond to  $\bar{\varepsilon} = 0.15$  for Yld2004-18p criterion (Barlat et al., 2005) with material orientation: (a)  $x^{\Sigma_{III}} y^{22.5^\circ} z^{22.5^\circ}$ , (b)  $x^{\Sigma_{III}} y^{45^\circ} z^{45^\circ}$  and (c)  $x^{\Sigma_{III}} y^{67.5^\circ} z^{67.5^\circ}$ . The origin of the Cartesian coordinate system  $(x'_1, x'_2, x'_3)$  is located at the center of mass of the void, with  $x'_1$ ,  $x'_2$  and  $x'_3$  being parallel to the loading axes  $x_1$ ,  $x_2$  and  $x_3$ , and also to the orthotropy axes  $x$ ,  $y$  and  $z$ . The initial diameter of the void is 1.

misalignments corresponds to  $y^{\Sigma_{III}} z^{\theta} x^{\theta}$ , and the greatest increase of  $f/f_0$  for large values of  $\theta$  to  $x^{\Sigma_{III}} y^{\theta} z^{\theta}$ . While the scale of the y-axis in the plots is bounded for the sake of clarity in the presentation of results, we have checked that the maximum value of normalized void volume fraction reached for  $x^{\Sigma_{III}} y^{\theta} z^{\theta}$  is  $f/f_0 \approx 12$  and it corresponds to  $\theta = 90^\circ$ , while in the cases of  $y^{\Sigma_{III}} z^{\theta} x^{\theta}$  and  $z^{\Sigma_{III}} x^{\theta} y^{\theta}$  it is  $f/f_0 \approx 12$  and  $\approx 10$ , respectively, and it corresponds to  $\theta = 0^\circ$ .

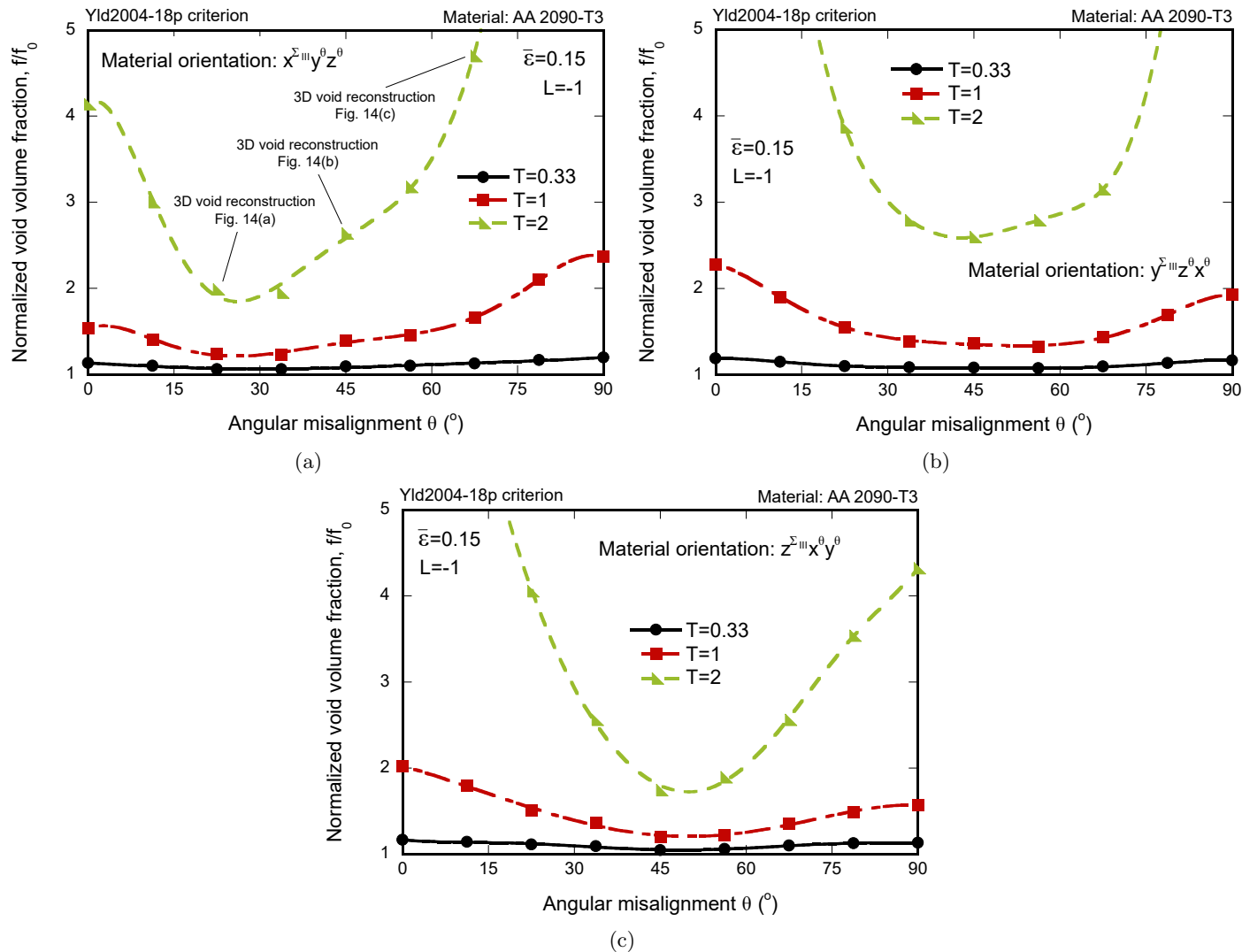


Figure 15: Influence of the macroscopic stress triaxiality on void growth for AA 2090-T3. Unit-cell finite element calculations for  $L = -1$  (axisymmetric tension) and three values of the stress triaxiality  $T = 0.33, 1$  and  $2$ . Evolution of the normalized void volume fraction  $f/f_0$  with the angular misalignment  $\theta$  for Yld2004-18p criterion (Barlat et al., 2005) and different material orientations: (a)  $x^{\Sigma_{III}} y^{\theta} z^{\theta}$ , (b)  $y^{\Sigma_{III}} z^{\theta} x^{\theta}$  and (c)  $z^{\Sigma_{III}} x^{\theta} y^{\theta}$ . The macroscopic effective strain is  $\bar{\epsilon} = 0.15$ .

Fig. 16 shows that for aluminum alloys 6111-T4 and 6013 the void growth is also strongly dependent of the angle  $\theta$ . In the case of the AA 6111-T4, the  $f/f_0 - \theta$  curve shows a local maximum for  $\theta \approx 45^\circ$  and two minima for  $\theta \approx 23^\circ$  and  $68^\circ$ , respectively. In the case of the AA 6013, the shape of the  $f/f_0 - \theta$  curve is different, such that the normalized void volume fraction first decreases, reaches a minimum, and then increases monotonically. Notice that the void volume

502 fraction is greater for aluminum alloy 6013 except for a small range of values of  $\theta$  spanning from  $\approx 36^\circ$  to  $\approx 52^\circ$ . These  
 503 results make apparent that the influence of angular misalignment on void growth is large and general, as it occurs for  
 504 different materials (compare also with the green dashed line in Fig. 15(a) which corresponds to AA 2090-T3 for the  
 505 same material orientation  $x^{\Sigma_{III}}y^\theta z^\theta$ , and the same values of effective strain, triaxiality and Lode parameter).

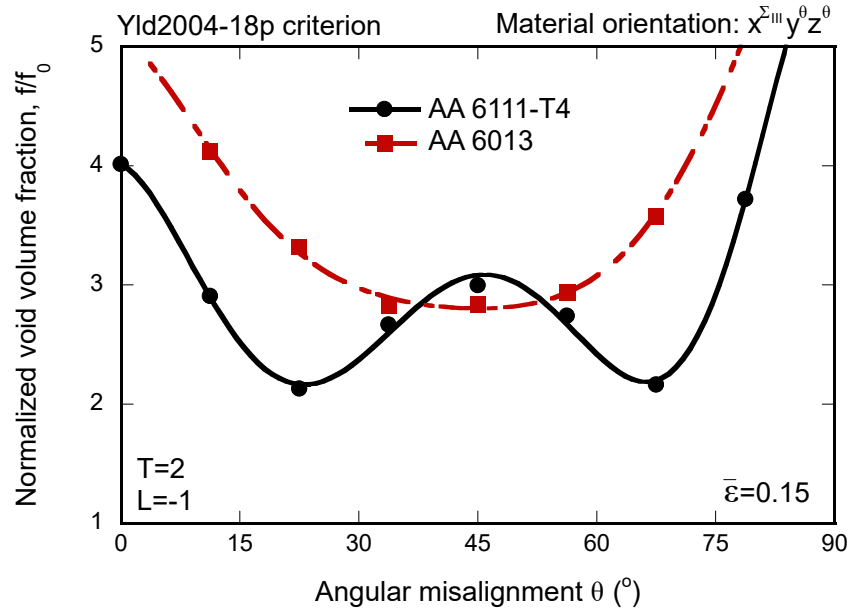


Figure 16: Comparison between results obtained for aluminum alloys 6111-T4 and 6013. Unit-cell finite element calculations for  $L = -1$  (axisymmetric tension) and  $T = 2$ . Evolution of the normalized void volume fraction  $f/f_0$  with the angular misalignment  $\theta$  for Yld2004-18p criterion (Barlat et al., 2005) and material orientation  $x^{\Sigma_{III}}y^\theta z^\theta$ . The macroscopic effective strain is  $\bar{\epsilon} = 0.15$ .

#### 506 4.2.2. The influence of Lode parameter

507 Fig. 17 shows the evolution of the normalized void volume fraction  $f/f_0$  with the macroscopic effective strain  $\bar{\epsilon}$  for  
 508 aluminium alloy 2090-T3, macroscopic triaxiality  $T = 1$  and two different values of the Lode parameter  $L = -1$  and  $0$ ,  
 509 which correspond to axisymmetric tension and generalized shear, respectively. Results are presented for Yld2004-18p  
 510 criterion for two different material orientations,  $x^{\Sigma_{III}}y^{22.5^\circ}z^{22.5^\circ}$  and  $x^{\Sigma_{III}}y^{67.5^\circ}z^{67.5^\circ}$ . While for  $x^{\Sigma_{III}}y^{22.5^\circ}z^{22.5^\circ}$  the  
 511 void grows faster for  $L = 0$  than for  $L = -1$ , the opposite behavior is obtained for  $x^{\Sigma_{III}}y^{67.5^\circ}z^{67.5^\circ}$ , making apparent the  
 512 interplay between the angular misalignment and the Lode parameter on void growth. Fig. 18 shows  $f/f_0 - \bar{\epsilon}$  curves for  
 513 the same macroscopic triaxiality and Lode parameter values, but different material orientations, namely  $y^{\Sigma_{III}}z^{22.5^\circ}x^{22.5^\circ}$   
 514 and  $y^{\Sigma_{III}}z^{67.5^\circ}x^{67.5^\circ}$ . The void grows faster for  $L = 0$  than for  $L = -1$ . However, while the results obtained for both  
 515 values of the Lode parameter are very similar for  $y^{\Sigma_{III}}z^{22.5^\circ}x^{22.5^\circ}$ , the differences increase for  $y^{\Sigma_{III}}z^{67.5^\circ}x^{67.5^\circ}$ , which  
 516 shows that the effect of the Lode parameter and the angular misalignment on the void volume fraction depends on the  
 517 material orientation.

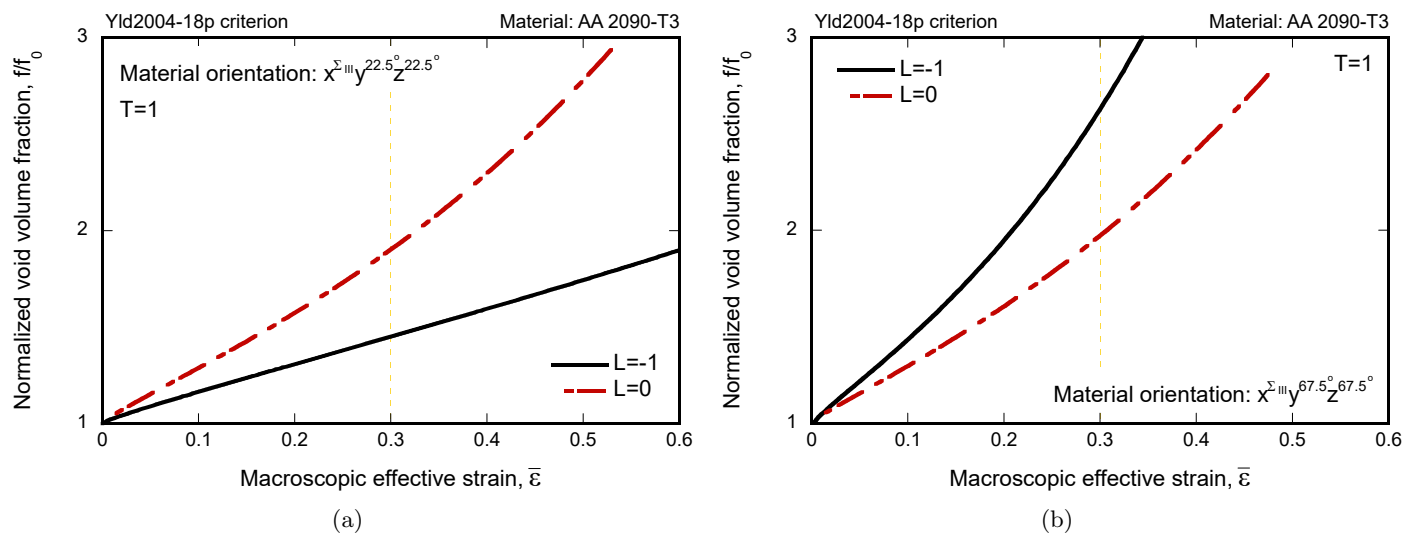


Figure 17: Influence of the macroscopic Lode parameter on void growth for AA 2090-T3. Unit-cell finite element calculations for two values of the Lode parameter  $L = -1$  and  $0$  (axisymmetric tension and generalized shear). Evolution of the normalized void volume fraction  $f/f_0$  with the macroscopic effective strain  $\bar{\epsilon}$ . The macroscopic triaxiality is  $T = 1$ . Results corresponding to Yld2004-18p yield criterion (Barlat et al., 2005) with material orientation: (a)  $x^{\Sigma} y^{22.5^{\circ}} z^{22.5^{\circ}}$  and (b)  $x^{\Sigma} y^{67.5^{\circ}} z^{67.5^{\circ}}$ . The dashed yellow line corresponds to the macroscopic effective strain  $\bar{\epsilon} = 0.3$ . (For interpretation of the references to color in this figure legend, the reader is referred to the web version of this article.)

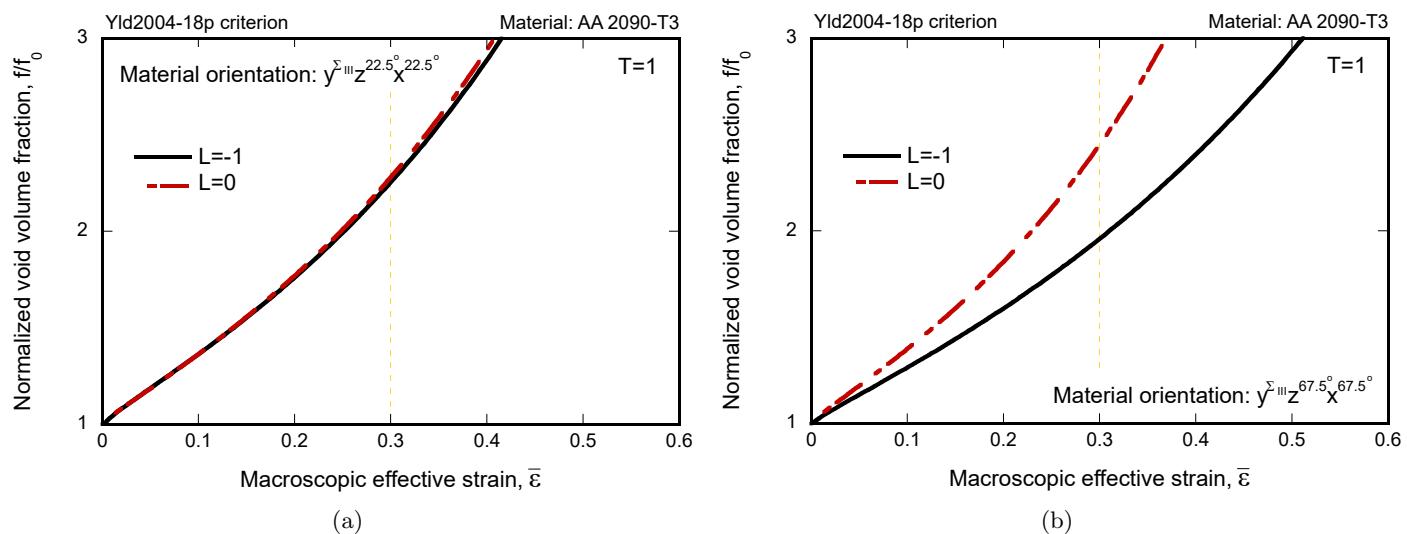


Figure 18: Influence of the macroscopic Lode parameter on void growth for AA 2090-T3. Unit-cell finite element calculations for two values of the Lode parameter  $L = -1$  and  $0$  (axisymmetric tension and generalized shear). Evolution of the normalized void volume fraction  $f/f_0$  with the macroscopic effective strain  $\bar{\epsilon}$ . The macroscopic triaxiality is  $T = 1$ . Results corresponding to Yld2004-18p yield criterion (Barlat et al., 2005) with material orientation: (a)  $y^{\Sigma} z^{22.5^{\circ}} x^{22.5^{\circ}}$  and (b)  $y^{\Sigma} z^{67.5^{\circ}} x^{67.5^{\circ}}$ . The dashed yellow line corresponds to the macroscopic effective strain  $\bar{\epsilon} = 0.3$ . (For interpretation of the references to color in this figure legend, the reader is referred to the web version of this article.)

Fig. 19 shows  $f/f_0 - \theta$  curves obtained for AA 2090-T3 and  $T = 1$  with different material orientations,  $x^{\Sigma_{III}}y^\theta z^\theta$  and  $y^{\Sigma_{III}}z^\theta x^\theta$ . As in Figs. 17 and 18, results are compared for two values of the Lode parameter,  $L = -1$  and  $L = 0$ . The macroscopic effective strain is  $\bar{\varepsilon} = 0.3$  (for this value of triaxiality the growth rate of the void is relatively low, so we select a high value of strain for the presentation of results). As in Fig. 15, the  $f/f_0 - \theta$  curves display a minimum void volume fraction for an intermediate value of  $\theta$ . The Lode parameter has an important impact on the evolution of the void volume fraction with the angular misalignment. Fig. 19(a) pictures the results for the material orientation  $x^{\Sigma_{III}}y^\theta z^\theta$ . The  $f/f_0 - \theta$  curves for  $L = -1$  and  $L = 0$  intersect at  $\theta \approx 45^\circ$ , so that for  $\theta < 45^\circ$  the greater void volume fraction corresponds to  $L = 0$ , and for  $\theta > 45^\circ$  to  $L = -1$ . The angular misalignment corresponding to the minimum void volume fraction also depends on the value of the Lode parameter, being  $\approx 22.5^\circ$  for  $L = -1$  and  $\approx 40^\circ$  for  $L = 0$ . Fig. 19(b) shows the results for  $y^{\Sigma_{III}}z^\theta x^\theta$ . The  $f/f_0 - \theta$  curves for  $L = -1$  and  $L = 0$  intersect at intermediate values of the angular misalignment, so that the void volume fraction corresponding to  $L = 0$  is greater within the range  $22.5^\circ < \theta < 80^\circ$ . These results stand in contrast with the calculations corresponding to  $x^{\Sigma_{III}}y^\theta z^\theta$  presented in Fig. 19(a), for which the void volume fraction for small values of  $\theta$  was greater for  $L = 0$ , and provide an example of the combined effect of Lode parameter, material orientation and angular misalignment on void growth.

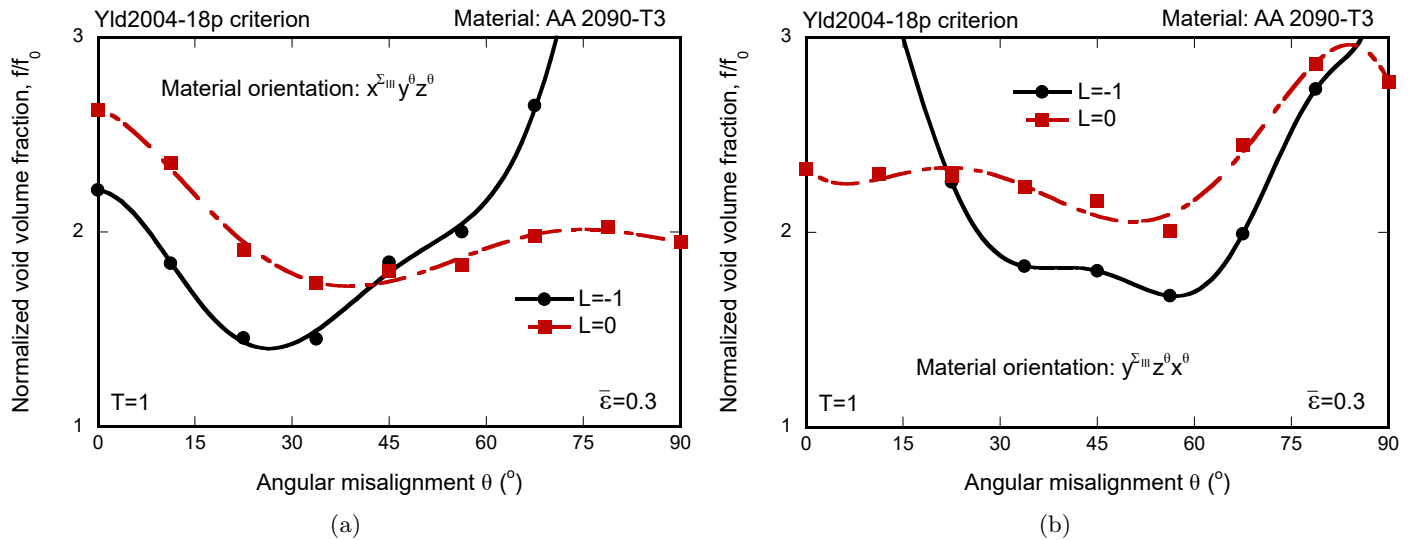


Figure 19: Influence of the macroscopic Lode parameter on void growth for AA 2090-T3. Unit-cell finite element calculations for  $T = 1$  and two values of the Lode parameter  $L = -1$  and  $0$  (axisymmetric tension and generalized shear). Evolution of the normalized void volume fraction  $f/f_0$  with the angular misalignment  $\theta$  for Yld2004-18p criterion (Barlat et al., 2005) and different material orientations: (a)  $x^{\Sigma_{III}}y^\theta z^\theta$  and (b)  $y^{\Sigma_{III}}z^\theta x^\theta$ . The macroscopic effective strain is  $\bar{\varepsilon} = 0.3$ .

Fig. 20 shows the same  $f/f_0 - \theta$  curves corresponding to aluminium alloy 6013. The void volume fraction displays a minimum for an intermediate value of the angular misalignment for both material orientations,  $x^{\Sigma_{III}}y^\theta z^\theta$  in Fig. 20(a) and  $y^{\Sigma_{III}}z^\theta x^\theta$  in Fig. 20(b), and for the two values of the Lode parameter considered. However, unlike in the case of AA 2090-T3, the void volume fraction is greater for axisymmetric tension ( $L = -1$ ) than for generalized shear ( $L = 0$ )

for the whole range of angular misalignments. These results show that the specific influence of the Lode parameter on the  $f/f_0 - \theta$  curves depends on both the material orientation and the angular misalignment, and varies from material to material.

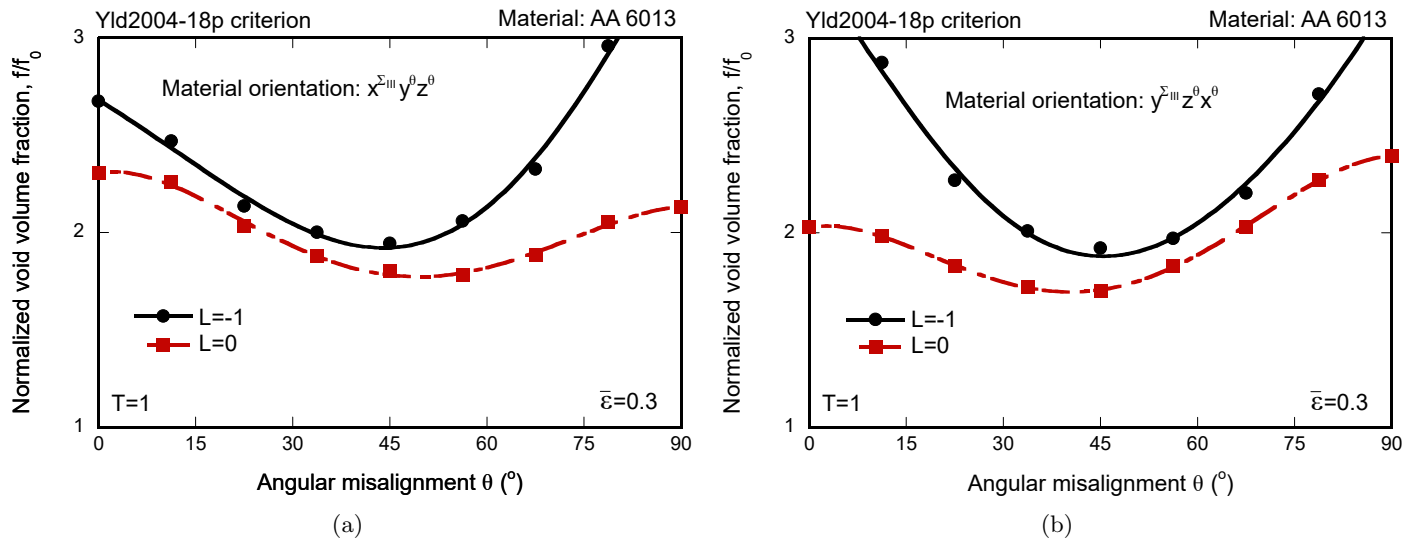


Figure 20: Influence of the macroscopic Lode parameter on void growth for AA 6013. Unit-cell finite element calculations for  $T = 1$  and two values of the Lode parameter  $L = -1$  and  $0$  (axisymmetric tension and generalized shear). Evolution of the normalized void volume fraction  $f/f_0$  with the angular misalignment  $\theta$  for Yld2004-18p criterion (Barlat et al., 2005) and different material orientations: (a)  $x^{\Sigma_{III}} y^{\theta} z^{\theta}$  and (b)  $y^{\Sigma_{III}} z^{\theta} x^{\theta}$ . The macroscopic effective strain is  $\bar{\epsilon} = 0.3$ .

#### 4.2.3. The influence of material orientation

Fig. 21 presents the normalized void volume fraction  $f/f_0$  versus the macroscopic effective strain  $\bar{\epsilon}$  for calculations performed for AA 2090-T3 with the Yld2004-18p yield criterion, for stress triaxiality  $T = 2$ , Lode parameter  $L = -1$  and different material orientations. The results pictured in Fig. 21(a) for  $x^{\Sigma_{III}} y^{22.5^\circ} z^{22.5^\circ}$ ,  $x^{\Sigma_{III}} y^{45^\circ} z^{45^\circ}$  and  $x^{\Sigma_{III}} y^{67.5^\circ} z^{67.5^\circ}$  show that within this range of angular misalignments the void grows faster as the angle  $\theta$  increases. However, the effect of  $\theta$  on void growth is different for the orientations  $z^{\Sigma_{III}} x^{22.5^\circ} y^{22.5^\circ}$ ,  $z^{\Sigma_{III}} x^{45^\circ} y^{45^\circ}$  and  $z^{\Sigma_{III}} x^{67.5^\circ} y^{67.5^\circ}$  shown in Fig. 21(b). Specifically, the curve corresponding to  $z^{\Sigma_{III}} x^{67.5^\circ} y^{67.5^\circ}$  lies between the results obtained for  $z^{\Sigma_{III}} x^{22.5^\circ} y^{22.5^\circ}$  and  $z^{\Sigma_{III}} x^{45^\circ} y^{45^\circ}$ , with the latter orientation displaying the lower growth rate of the void. Consistent with the results shown in Section 4.2.2, these calculations reinforce the idea that the effect of the angular misalignment on void growth depends on the material orientation.

Moreover, the influence of the material orientation on the evolution of the shape and the size of the void during loading is illustrated in Figs. 22 and 23, which picture 3D reconstructions of the voids for the orientations  $x^{\Sigma_{III}} y^{45^\circ} z^{45^\circ}$  and  $z^{\Sigma_{III}} x^{45^\circ} y^{45^\circ}$ , respectively, for different values of the macroscopic effective strain  $\bar{\epsilon} = 0.03, 0.13, 0.23$  and  $0.35$  (indicated with yellow markers in Figs. 21(a) and 21(b)). As the loading progresses, the voids, initially spherical, grow and twist, evolving towards a deformed shape that is not ellipsoidal (as anticipated in the first paragraph of Section

4.2). In addition, the comparison of Figs. 22 and 23 makes apparent that the void grows faster for the orientation  
 $x^{\Sigma_{III}}y^{45^\circ}z^{45^\circ}$  (as also shown in Fig. 21). Twisting and rotation of void and unit-cell (anticipated in the first paragraph  
of Section 4.2) is further illustrated in Fig. 24, which shows contours of effective plastic strain for the calculations  
presented in Figs. 22 and 23 for a macroscopic effective strain of 0.35. The contour plots correspond to the cut-view  
 $x_3 = \frac{L_0}{2}$  (mid-plane of the unit-cell) and the color coding is such that effective plastic strains ranging from 0 to 0.5  
correlate with a color scale that goes from blue to red. If the value of the effective plastic strain is above 0.5, it remains  
red. The plots bring out the non-planar profile of the faces of the uni-cell (initially straight sides become curved), and  
the fact that the effective plastic strain fields are not symmetric with respect to the loading axes (recall that the effective  
plastic strain fields in the calculations shown in Fig. 5 were symmetric with respect to the loading axes). The deformed  
shape of the unit-cell also makes apparent the effect of the periodic boundary conditions enforcing coupled displacement  
of material points belonging to opposed faces.

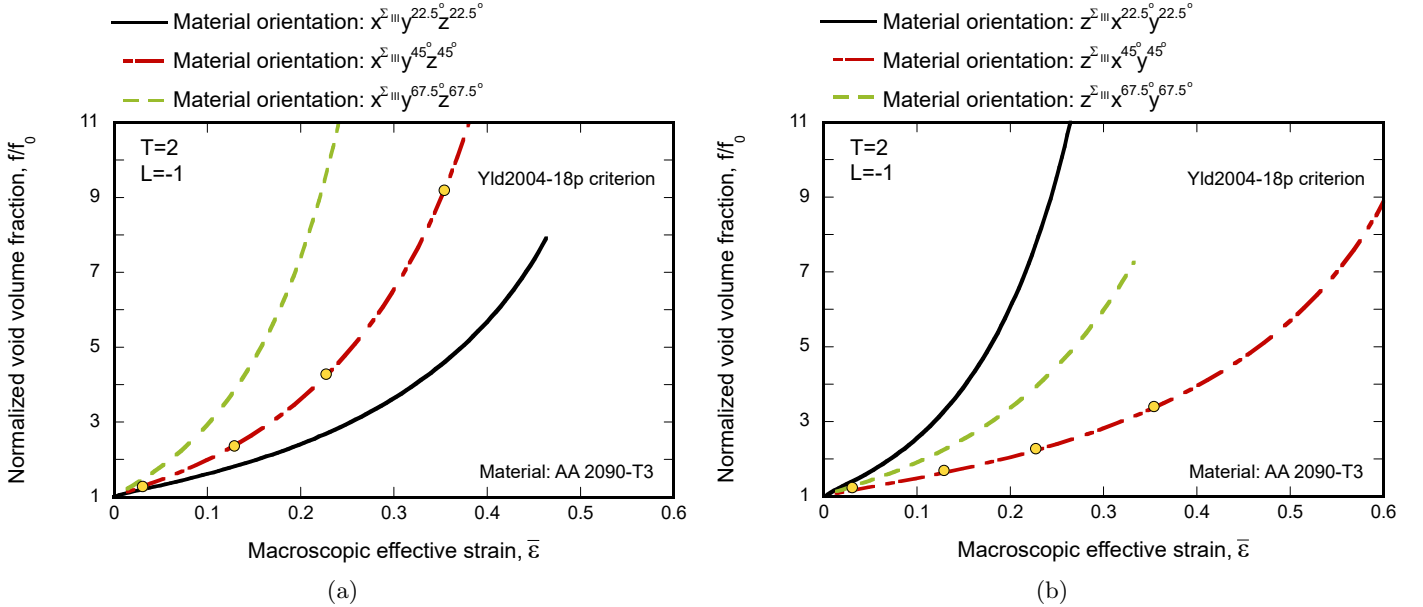


Figure 21: Influence of the material orientation on void growth for AA 2090-T3. Evolution of the normalized void volume fraction  $f/f_0$  with the macroscopic effective strain  $\bar{\epsilon}$ . Unit-cell finite element calculations for Yld2004-18p yield criterion (Barlat et al., 2005) with stress triaxiality  $T = 2$ , Lode parameter  $L = -1$  (axisymmetric tension), and different material orientations. (a)  $x^{\Sigma_{III}}y^{22.5^\circ}z^{22.5^\circ}$ ,  $x^{\Sigma_{III}}y^{45^\circ}z^{45^\circ}$ , and  $x^{\Sigma_{III}}y^{67.5^\circ}z^{67.5^\circ}$ , (b)  $z^{\Sigma_{III}}x^{22.5^\circ}y^{22.5^\circ}$ ,  $z^{\Sigma_{III}}x^{45^\circ}y^{45^\circ}$  and  $z^{\Sigma_{III}}x^{67.5^\circ}y^{67.5^\circ}$ . (For interpretation of the references to color in this figure legend, the reader is referred to the web version of this article.)

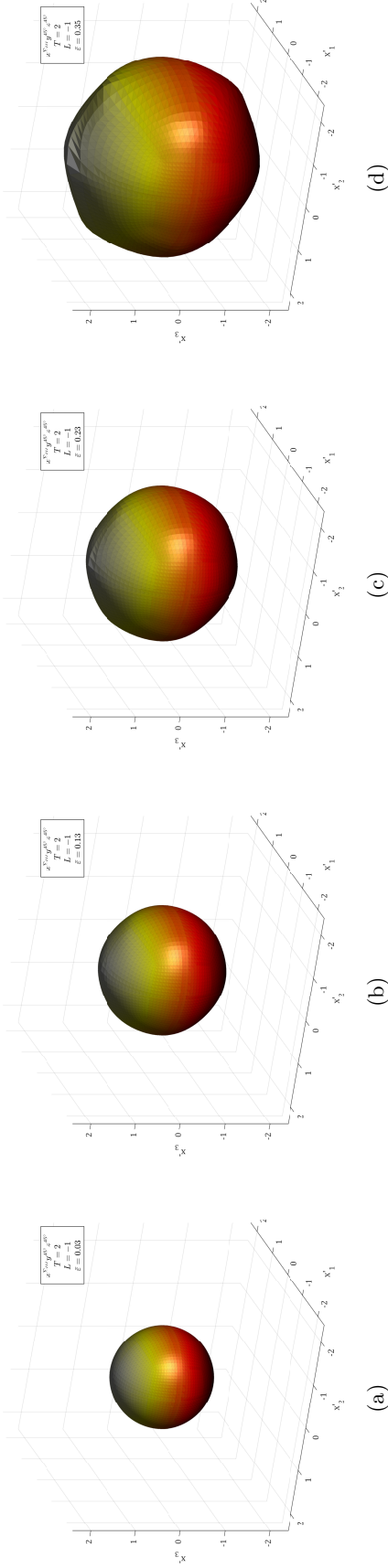


Figure 22: 3D reconstruction of the surface of the void for AA 2090-T3 and different values of the macroscopic effective strain: (a)  $\bar{\varepsilon} = 0.03$ , (b)  $\bar{\varepsilon} = 0.13$ , (c)  $\bar{\varepsilon} = 0.23$  and (d)  $\bar{\varepsilon} = 0.35$ . Results corresponding to Yld2004-18p criterion (Barlat et al., 2005) with material orientation  $x^{\Sigma III} y^{45^\circ} z^{45^\circ}$ . The macroscopic triaxiality is  $T = 2$  and the Lode parameter is  $L = -1$  (axisymmetric tension). The origin of the Cartesian coordinate system  $(x'_1, x'_2, x'_3)$  is located at the center of mass of the void, with  $x'_1, x'_2$  and  $x'_3$  being parallel to the loading axes  $x_1, x_2$  and  $x_3$ . The initial diameter of the void is 1.

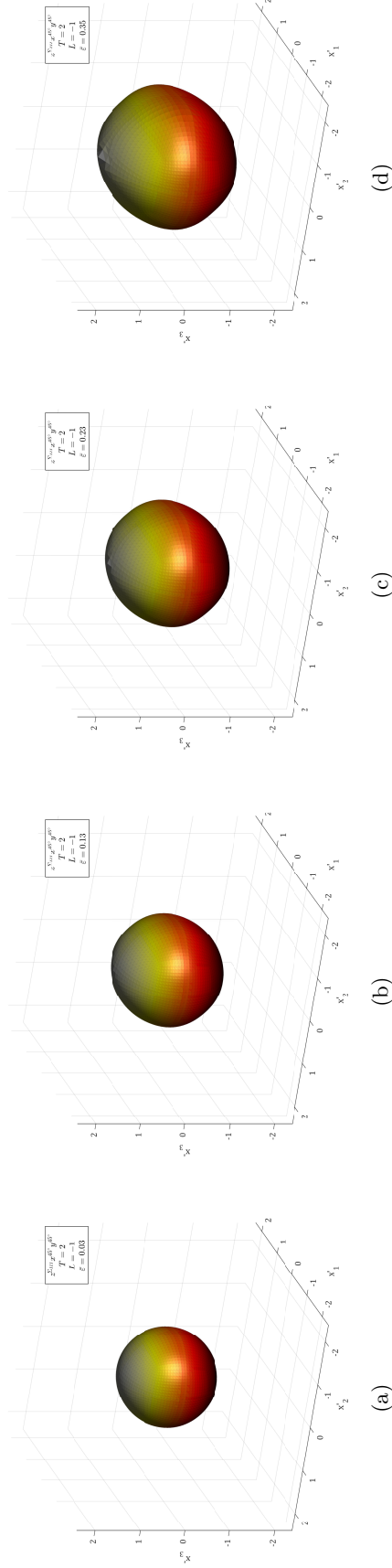


Figure 23: 3D reconstruction of the surface of the void for AA 2090-T3 and different values of the macroscopic effective strain: (a)  $\bar{\varepsilon} = 0.03$ , (b)  $\bar{\varepsilon} = 0.13$ , (c)  $\bar{\varepsilon} = 0.23$  and (d)  $\bar{\varepsilon} = 0.35$ . Results corresponding to Yld2004-18p criterion (Barlat et al., 2005) with material orientation  $z^{\Sigma III} x^{45^\circ} y^{45^\circ}$ . The macroscopic triaxiality is  $T = 2$  and the Lode parameter is  $L = -1$  (axisymmetric tension). The origin of the Cartesian coordinate system  $(x'_1, x'_2, x'_3)$  is located at the center of mass of the void, with  $x'_1, x'_2$  and  $x'_3$  being parallel to the loading axes  $x_1, x_2$  and  $x_3$ . The initial diameter of the void is 1.

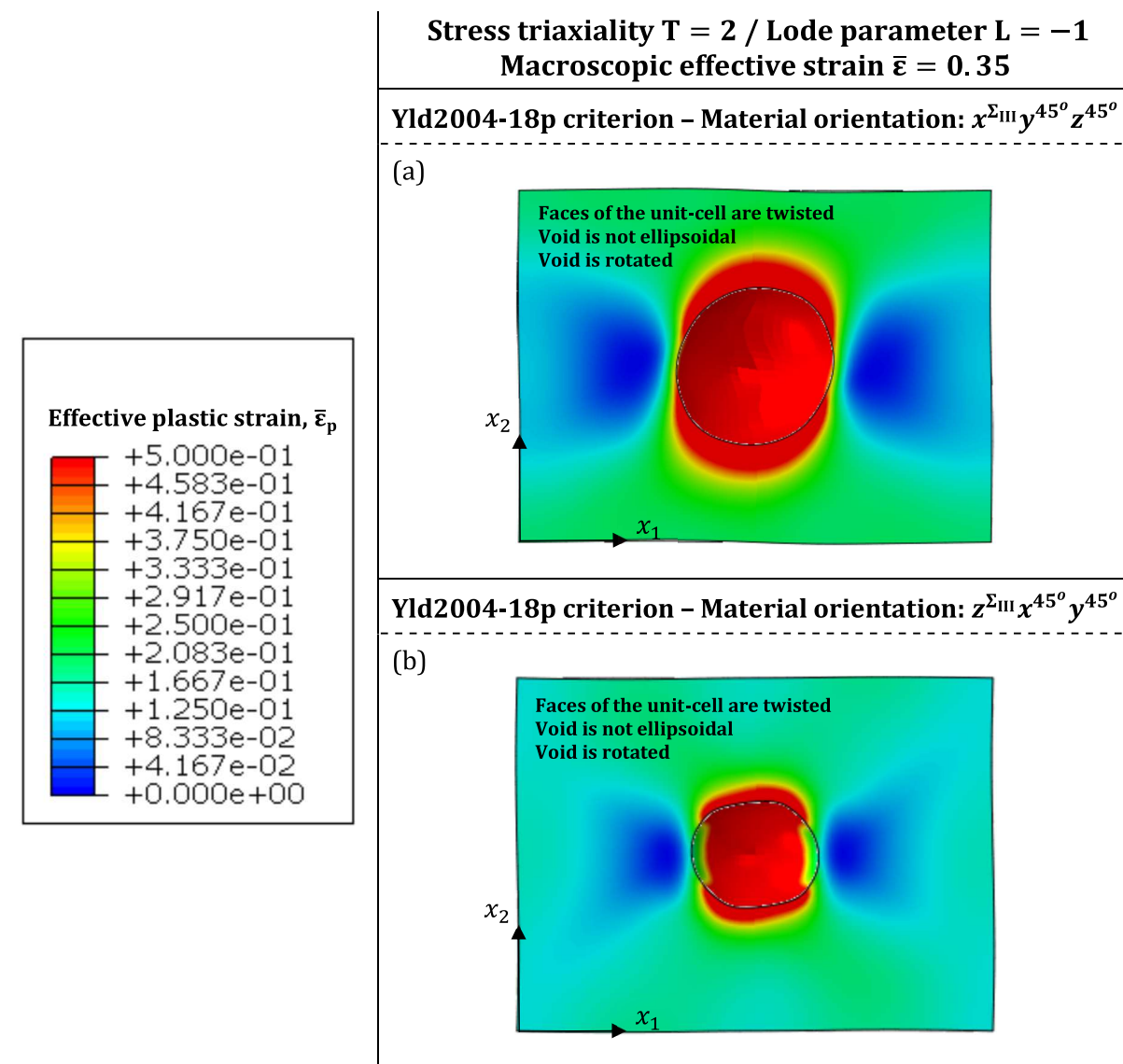


Figure 24: Influence of the material orientation on void growth for AA 2090-T3. Contours of effective plastic strain in the matrix material  $\bar{\epsilon}_p$  for unit-cell finite element calculations performed with macroscopic triaxiality  $T = 2$  and Lode parameter  $L = -1$  (axisymmetric tension). Cut-view for  $x_3 = L_0/2$ . The macroscopic effective strain is  $\bar{\epsilon} = 0.35$ . Results corresponding to Yld2004-18p criterion (Barlat et al., 2005) with material orientation: (a)  $x^{\Sigma_{III}}y^{45^\circ}z^{45^\circ}$  and (b)  $z^{\Sigma_{III}}x^{45^\circ}y^{45^\circ}$ .

567

568 Fig. 25 compares the evolution of the normalized void volume fraction  $f/f_0$  with the angular misalignment  $\theta$  for  
569 calculations performed for AA 2090-T3 with different material orientations,  $x^{\Sigma_{III}}y^\theta z^\theta$ ,  $y^{\Sigma_{III}}z^\theta x^\theta$  and  $z^{\Sigma_{III}}x^\theta y^\theta$ . Results  
570 are shown for two values of the stress triaxiality,  $T = 1$  and  $T = 2$ , in Figs. 25(a) and 25(b), respectively. Notice that in  
571 Fig. 25(b) the scale of the ordinate axis is three times greater than in the case of  $T = 1$  due to faster void growth with  
572 increasing triaxiality. The Lode parameter is  $L = 0$ , and the macroscopic effective strain is 0.3 in Fig. 25(a) and 0.15 in  
573 Fig. 25(b), respectively. The evolution of the void volume fraction  $f/f_0$  with  $\theta$  displays a minimum for an intermediate  
574 value of the angular misalignment (just like in Figs. 15 and 19 for different values of the Lode parameter and stress

575 triaxiality). The  $f/f_0 - \theta$  curves obtained for different orientations intersect each other, with the smallest value of  $f/f_0$   
 576 corresponding to  $z^{\Sigma_{III}}x^\theta y^\theta$ , illustrating that the specific effect of material orientation on void growth depends on both  
 577 stress state and angular misalignment.

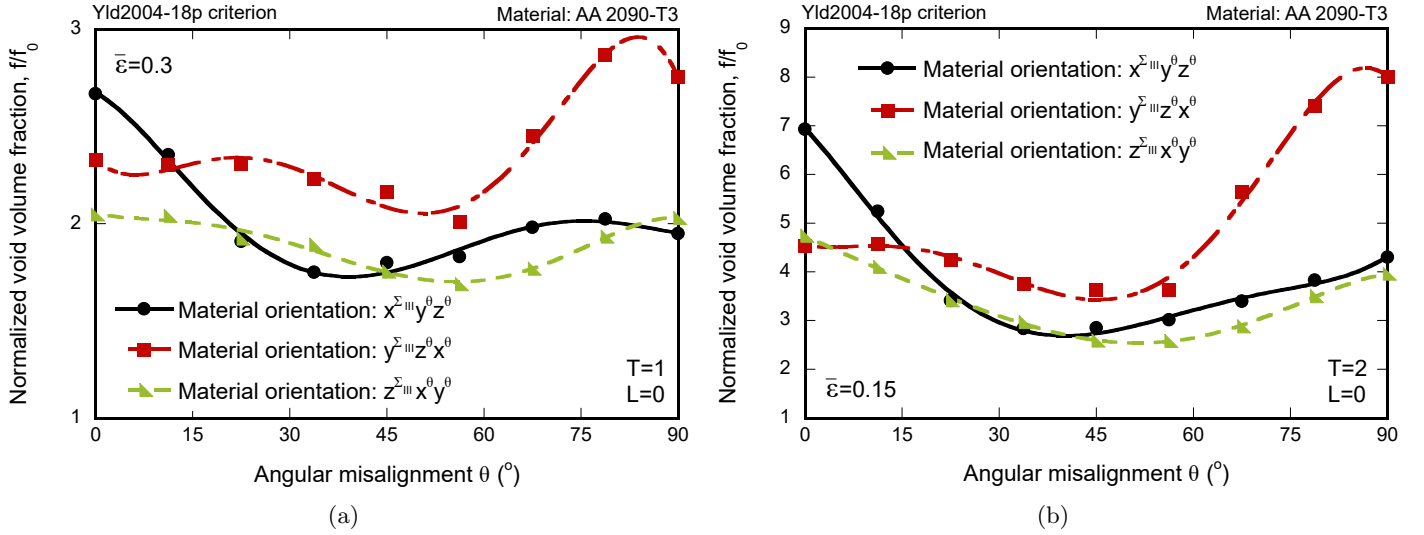


Figure 25: Influence of the material orientation on void growth for AA 2090-T3. Unit-cell finite element calculations for Yld2004-18p criterion (Barlat et al., 2005) with material orientations  $x^{\Sigma_{III}}y^\theta z^\theta$ ,  $y^{\Sigma_{III}}z^\theta x^\theta$  and  $z^{\Sigma_{III}}x^\theta y^\theta$ . Evolution of the normalized void volume fraction  $f/f_0$  with the angular misalignment  $\theta$ . The value of the Lode parameter is  $L = 0$  (generalized shear). Macroscopic stress triaxiality and macroscopic effective strain: (a)  $T = 1$  and  $\bar{\epsilon} = 0.3$ , (b)  $T = 2$  and  $\bar{\epsilon} = 0.15$ .

578

579 Fig. 26 shows  $f/f_0 - \theta$  curves for AA 2090-T3 corresponding to material orientations  $x^{\Sigma_I}y^\theta z^\theta$ ,  $y^{\Sigma_I}z^\theta x^\theta$  and  $z^{\Sigma_I}x^\theta y^\theta$ ,  
 580 so that the major loading direction  $x_1$  is aligned with one anisotropy axis ( $x$ ,  $y$  and  $z$ , respectively), and the other  
 581 two loading directions form an angle  $\theta$  with the second and third anisotropy axes. The macroscopic stress triaxiality is  
 582  $T = 2$ .

583 Fig. 26(a) pictures results for  $L = -1$  (axisymmetric tension) and  $\bar{\epsilon} = 0.1$ . Unlike the results shown in Figs. 15,  
 584 16, 19, 20 and 25, the normalized void volume fraction for  $x^{\Sigma_I}y^\theta z^\theta$  shows a maximum, instead of a minimum, for an  
 585 intermediate value of the angular misalignment. On the other hand, for  $y^{\Sigma_I}z^\theta x^\theta$  and  $z^{\Sigma_I}x^\theta y^\theta$ , the  $f/f_0 - \theta$  curves are  
 586 nearly horizontal, i.e., the angular misalignment has a small effect on the void volume fraction. The shape of the  
 587  $f/f_0 - \theta$  curves is different for the results presented in Fig. 26(b) for the Lode parameter  $L = 0$  (generalized shear)  
 588 and the effective strain  $\bar{\epsilon} = 0.15$ , such that the void volume fraction shows a minimum for an intermediate value of  
 589 the angular misalignment, as in Figs. 15, 16, 19, 20 and 25. The lowest void growth corresponds to the orientation  
 590  $x^{\Sigma_I}y^\theta z^\theta$ . These results show the influence of the orientation of the minor and major loading directions with respect to  
 591 the anisotropy axes of the material, bringing to light that it is possible to find both a minimum and a maximum of  $f/f_0$   
 592 for angular misalignments within the range  $0^\circ < \theta < 90^\circ$ .

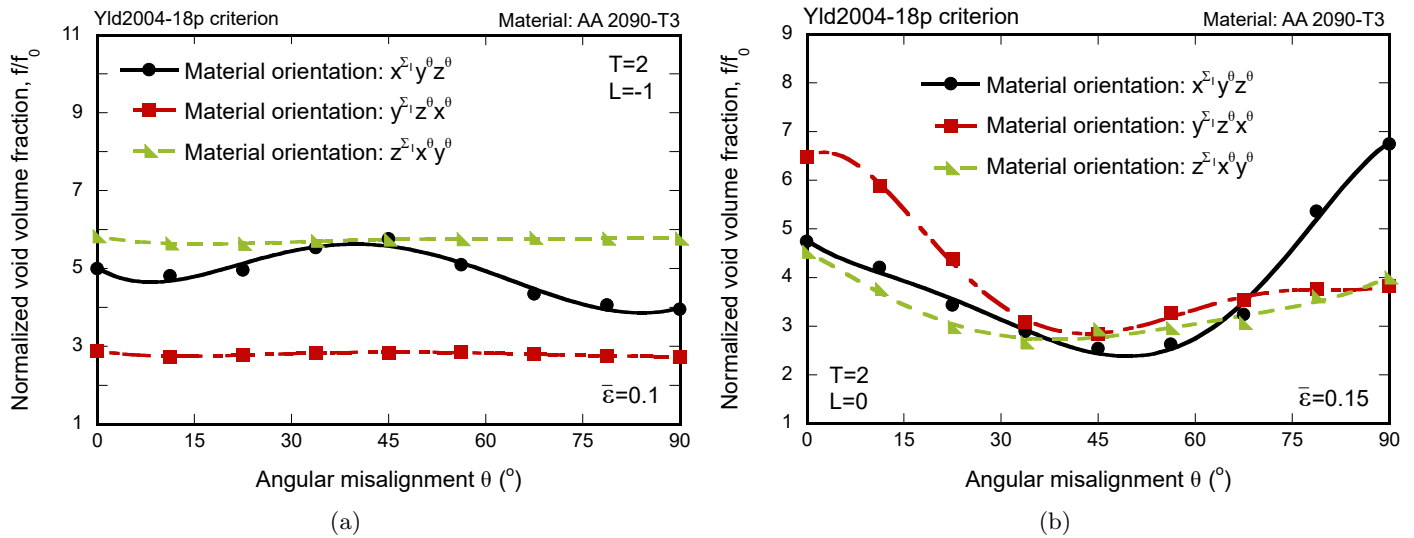


Figure 26: Influence of the material orientation on void growth for AA 2090-T3. Unit-cell finite element calculations for Yld2004-18p yield criterion (Barlat et al., 2005) with material orientations  $x^{\Sigma_1} y^{\theta} z^{\theta}$ ,  $y^{\Sigma_1} z^{\theta} x^{\theta}$  and  $z^{\Sigma_1} x^{\theta} y^{\theta}$ . Evolution of the normalized void volume fraction  $f/f_0$  with the angular misalignment  $\theta$ . The macroscopic stress triaxiality is  $T = 2$ . The Lode parameter and the macroscopic effective strain are: (a)  $L = -1$  (axisymmetric tension) and  $\bar{\epsilon} = 0.1$ , (b)  $L = 0$  (generalized shear) and  $\bar{\epsilon} = 0.15$ .

## 5. Summary and concluding remarks

In this paper, we have performed a finite element analysis to identify the role of plastic anisotropy on void growth in three aluminium alloys: 2090-T3, 6111-T4 and 6013. For that task, we have assumed that the material displays a periodic porous microstructure that can be approximated by an array of representative volume elements idealized as cubic unit-cells with a spherical void located at their center and subjected to periodic boundary conditions. The unit-cell model has been implemented in ABAQUS/Standard (2016), with the behavior of the matrix material being described with an elastic isotropic, plastic orthotropic constitutive model with yielding defined by the Yld2004-18p criterion (Barlat et al., 2005) in which anisotropy is introduced through 2 linear transformations of the stress deviator which provide 18 anisotropy coefficients. The constitutive model has been included in the environment of ABAQUS/Standard (2016) through a UMAT subroutine, using the stress integration algorithm based on the numerical approximation of the yield function gradients developed by Hosseini and Rodríguez-Martínez (2021). Moreover, the multi-point constraint subroutine developed by Dakshinamurthy et al. (2021) has been used to enforce constant values of macroscopic stress triaxiality  $T$  and Lode parameter  $L$  in unit-cell calculations that have been carried out for  $T = 0.33, 1$  and  $2$ , and  $L = -1, 0$  and  $1$ .

Firstly, following the recent work of Bryhni Dæhli et al. (2017a), we have considered the loading directions being parallel to the orthotropy axes of the material, so that the principal directions of macroscopic stress and macroscopic strain coincide. A key feature of the analysis is that we have rotated the Cartesian coordinate system formed by the

material orthotropy axes to perform calculations in which the minor loading axis of the unit-cell corresponds either with the rolling, the transverse or the normal direction. In addition, the finite element results obtained for the anisotropic material have been systematically compared with simulations carried out using isotropic von Mises (1928) plasticity.

The main outcomes of this analysis are as follows:

- As expected, the general trend is that the increase of triaxiality speeds up the growth rate of the void. However, the void volume evolution depends on the material anisotropy, so that the void grows faster or slower than in the isotropic case depending on the triaxiality and the orientation of the material orthotropy axes.
- The numerical results have shown that for specific material orientations, the anisotropy switches the effect of the Lode parameter on void growth, reversing the trends obtained for the isotropic von Mises material.
- 3D reconstruction of the voids geometry during loading using a Quickhull algorithm has revealed that the initially spherical void turns into an ellipsoid whose rate of growth and eccentricity depend on stress triaxiality, Lode parameter and material orientation. In fact, consistent with the results of Bryhni Dæhli et al. (2017a), we have shown that the void shape evolves quite differently depending upon the orientation of the minor loading direction relative to the material axes.

Secondly, we have devised a novel strategy to perform calculations considering angular misalignments within the range  $0^\circ \leq \theta \leq 90^\circ$ , so that one loading direction is parallel to one of the symmetry axes of the material, and  $\theta$  is the angle formed between the other two loading directions and the second and third orthotropy axes. Note that the symmetry of the material with respect to the orthotropy axes makes the response of the cell the same for  $\pm\theta$ . These numerical results constitute the main original contribution of this work. In fact, to the authors' knowledge, these are the first unit-cell calculations ever reported in which the material is modeled using a macroscopic anisotropic yield function with prescribed misalignment between loading and material axes and, at the same time, the macroscopic stress triaxiality and the Lode parameter are controlled to be constant during loading. The main outcomes of this analysis are as follows:

- The calculations performed for the three aluminium alloys –2090-T3, 6111-T4 and 6013– bring out that the evolution of the growth rate of the void with the angular misalignment is generally strongly nonlinear, so that there is an intermediate value of the angle  $\theta$  for which the growth rate of the void reaches an extreme value (minimum or maximum) which depends on the material orientation and on the Lode parameter.
- The greater the stress triaxiality, the greater the influence of the angular misalignment on void growth, with the specific influence of the Lode parameter being dependent on the material orientation.

- The misalignment between loading and material axes makes that the initially straight sides of the unit-cell become curved, and the voids are no longer ellipsoidal, and rotate and twist during loading.

These results suggest that material orientation can be exploited to control void growth and thus promote or delay localization and fracture of anisotropic metal products.

In addition, we have performed selected calculations for AA 2090-T3 with two other advanced yield criteria, CPB06ex2 (Plunkett et al., 2008) and Yld2011-27p (Aretz and Barlat, 2013), specifically calibrated to model the behavior of AA 2090-T3. The comparison carried out in Appendix A with the results obtained with the Yld2004-18p criterion has brought out that different constitutive models, while calibrated for the same specific material, lead to different predictions for the evolution of the shape and the size of the void, and also for the distribution of plastic strains near the void. Nevertheless, we are aware that a more thorough analysis should be performed in future work to substantiate this conclusion. We also leave for future work to extend the range of triaxiality values investigated in this paper, with the aim of studying void evolution in anisotropic materials under shear dominated loadings.

## Acknowledgements

The research leading to these results has received funding from the European Research Council (ERC) under the European Union’s Horizon 2020 research and innovation programme. Project PURPOSE, grant agreement 758056.

The authors express sincere gratitude to Dr. Oana Cazacu (University of Florida) for helpful discussions on plastic anisotropy of metallic materials.

## Appendix A. The influence of constitutive model

We compare calculations for aluminium alloy 2090-T3 performed using the constitutive framework presented in Section 2 with finite element results obtained with the yield criteria CPB06ex2 (Plunkett et al., 2008) and Yld2011-27p (Aretz and Barlat, 2013). The CPB06ex2 model accounts for both the anisotropy and tension-compression asymmetry of the material, which are introduced using 2 linear transformations of the stress deviator. The CPB06ex2 yield criterion contains 18 parameters to describe the anisotropy and 2 for the tension-compression asymmetry. The Yld2011-27p model does not consider the tension-compression asymmetry of the material, and the anisotropy is introduced using 3 linear transformations of the stress deviator, which results in 27 anisotropy coefficients, thereby providing extended flexibility to capture the mechanical response of materials with complex anisotropic behaviour. We have implemented

both CPB06ex2 and Yld2011-27p yield criteria in ABAQUS/Standard (2016) through a UMAT subroutine using the integration scheme reported in Hosseini and Rodríguez-Martínez (2021). In the finite element calculations we use the material parameters reported by Plunkett et al. (2008) and Aretz and Barlat (2013).

Fig. A.27 compares  $f/f_0 - \bar{\epsilon}$  curves obtained with Yld2004-18p, CPB06ex2 and Yld2011-27p yield criteria, for stress triaxiality  $T = 2$  and Lode parameter  $L = 1$ . Loading and orthotropy axes are parallel. Results are shown for different material orientations:  $x^{\Sigma_{III}} y^{\Sigma_I} z^{\Sigma_{II}}$ ,  $y^{\Sigma_{III}} z^{\Sigma_I} x^{\Sigma_{II}}$  and  $z^{\Sigma_{III}} x^{\Sigma_I} y^{\Sigma_{II}}$ . The rate of growth of the void is significantly affected by the specific constitutive model used to describe the behavior of the matrix material, so that for any given value of the macroscopic strain, the greatest void volume fraction corresponds to the Yld2004-18p criterion, and the smallest to the CPB06ex2 model. Notice also that the differences in the predictions obtained with the three constitutive models depend on the material orientation, e.g., the rate of growth of the void is more sensitive to the constitutive model for  $x^{\Sigma_{III}} y^{\Sigma_I} z^{\Sigma_{II}}$  than for  $y^{\Sigma_{III}} z^{\Sigma_I} x^{\Sigma_{II}}$  and  $z^{\Sigma_{III}} x^{\Sigma_I} y^{\Sigma_{II}}$ .

Fig. A.28 shows the evolution of the void volume fraction  $f/f_0$  with the macroscopic effective strain  $\bar{\epsilon}$  for calculations performed with Yld2004-18p, CPB06ex2 and Yld2011-27p yield criteria. The stress triaxiality is  $T = 2$  and the Lode parameter  $L = -1$ . Results are shown for  $z^{\Sigma_{III}} x^{22.5^\circ} y^{22.5^\circ}$ ,  $z^{\Sigma_{III}} x^{45^\circ} y^{45^\circ}$  and  $z^{\Sigma_{III}} x^{67.5^\circ} y^{67.5^\circ}$ . The results are qualitatively the same presented in Fig. A.27, with the greatest and the smallest growth rate of the void corresponding to Yld2004-18p and CPB06ex2 models, respectively. These results bring out that the influence of the constitutive model on the evolution of the void is general, as long as it is observed for different loading conditions and material orientations. Moreover, Fig. A.29 shows contours of effective plastic strain for the calculations presented in Fig. 28(b) corresponding to CPB06ex2 and Yld2011-27p yield criteria. The macroscopic effective strain is 0.35. The contour plots correspond to the cut-view  $x_3 = \frac{L_0}{2}$  (mid-plane of the unit-cell) and the color coding is the same used in Fig. 24 so that the results can be directly compared with the contour plots shown therein for the orientation  $z^{\Sigma_{III}} x^{45^\circ} y^{45^\circ}$ . The yield criterion is shown to affect the size and the shape of the void, and also the fields of equivalent plastic strain that develop near the void. Notice that the greatest plastically deformed zone corresponds to the model Yld2004-18p (see Fig. 24) and the smallest to the CPB06ex2 yield function (check the extension of the red area).

While the general trends obtained with the three constitutive models are the same for the loading cases considered, this Appendix brings to light that using different yield criteria, despite they are calibrated for the same material, lead to important quantitative differences in the results for the void evolution obtained with the unit-cell model, and thus to different predictions for the development of plastic localization and damage in the material.

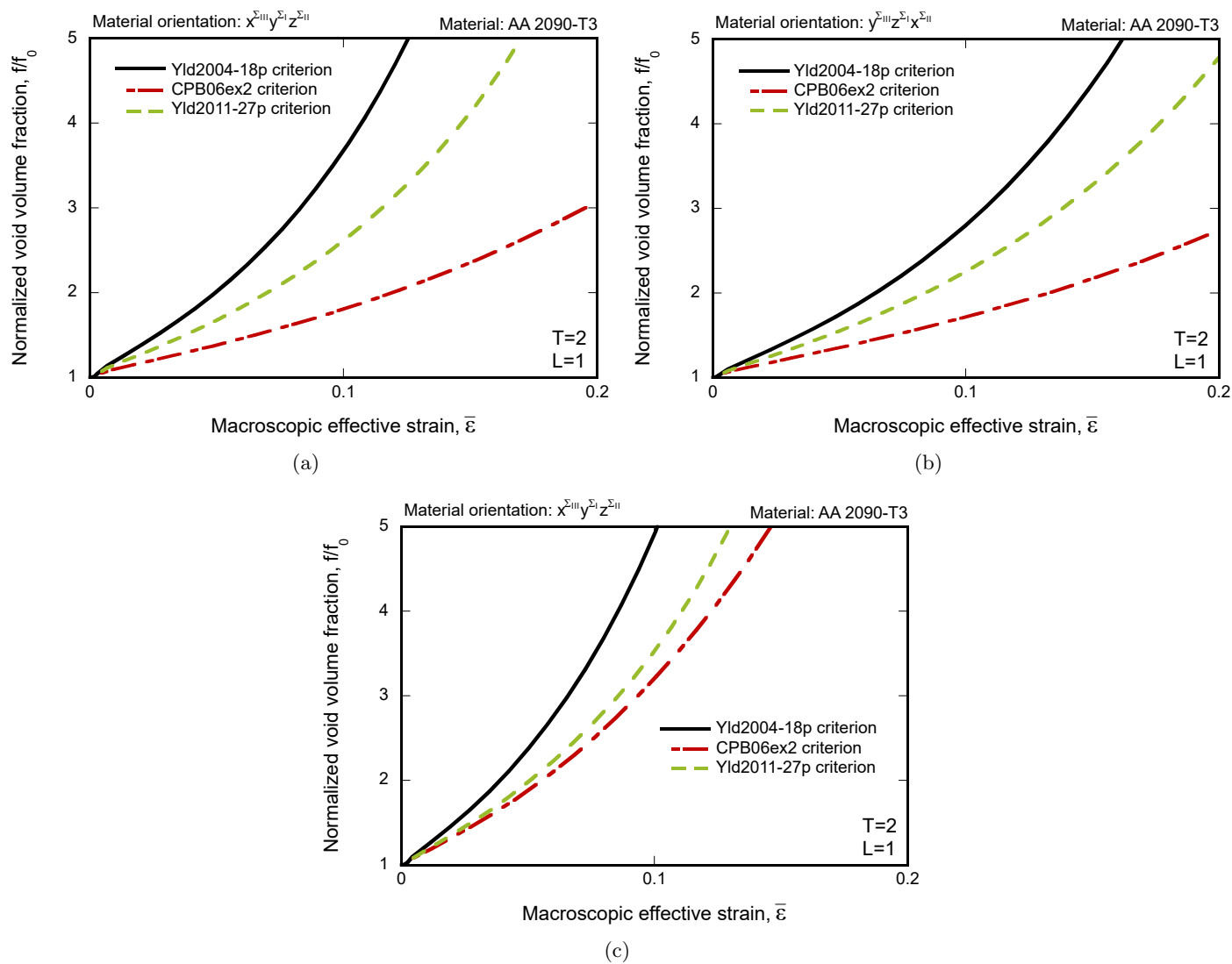


Figure A.27: Influence of the constitutive model on void growth for AA 2090-T3. Evolution of the normalized void volume fraction  $f/f_0$  with the macroscopic effective strain  $\bar{\epsilon}$ . Stress triaxiality  $T = 2$  and Lode parameter  $L = 1$  (axisymmetric compression). Comparison of unit-cell finite element calculations performed with Yld2004-18p (Barlat et al., 2005), CPB06ex2 (Plunkett et al., 2008) and Yld2011-27p (Aretz and Barlat, 2013) yield criteria for different material orientations: (a)  $x^{\Sigma_{III}} y^{\Sigma_{I}} z^{\Sigma_{II}}$ , (b)  $y^{\Sigma_{III}} z^{\Sigma_{I}} x^{\Sigma_{II}}$  and (c)  $z^{\Sigma_{III}} x^{\Sigma_{I}} y^{\Sigma_{II}}$ .

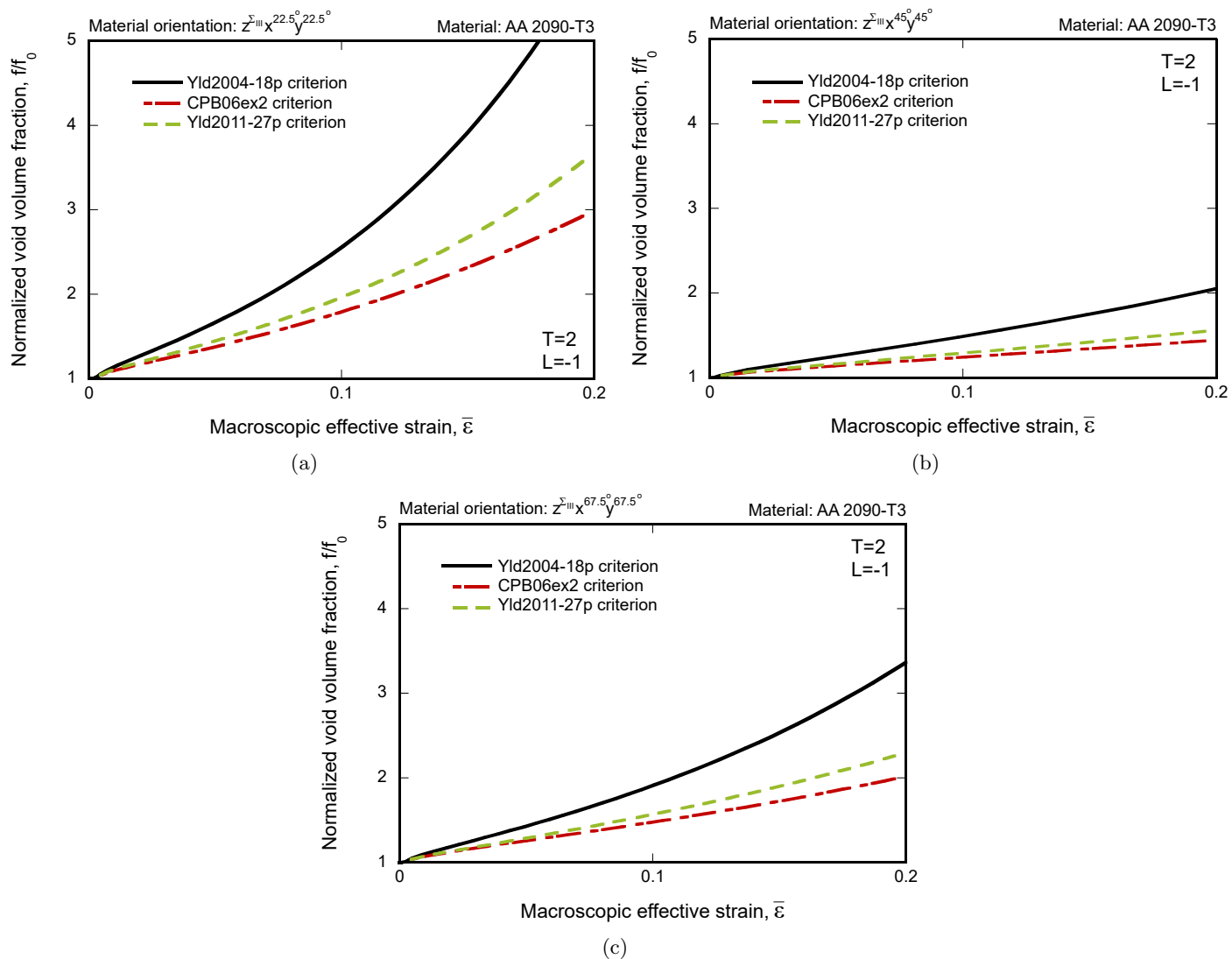


Figure A.28: Influence of the constitutive model on void growth for AA 2090-T3. Evolution of the normalized void volume fraction  $f/f_0$  with the macroscopic effective strain  $\bar{\epsilon}$ . Stress triaxiality  $T = 2$  and Lode parameter  $L = -1$  (axisymmetric tension). Comparison of unit-cell finite element calculations performed with Yld2004-18p (Barlat et al., 2005), CPB06ex2 (Plunkett et al., 2008) and Yld2011-27p (Aretz and Barlat, 2013) yield criteria for different material orientations: (a)  $z^{\text{III}}x^{22.5^\circ}y^{22.5^\circ}$ , (b)  $z^{\text{III}}x^{45^\circ}y^{45^\circ}$  and (c)  $z^{\text{III}}x^{67.5^\circ}y^{67.5^\circ}$ .

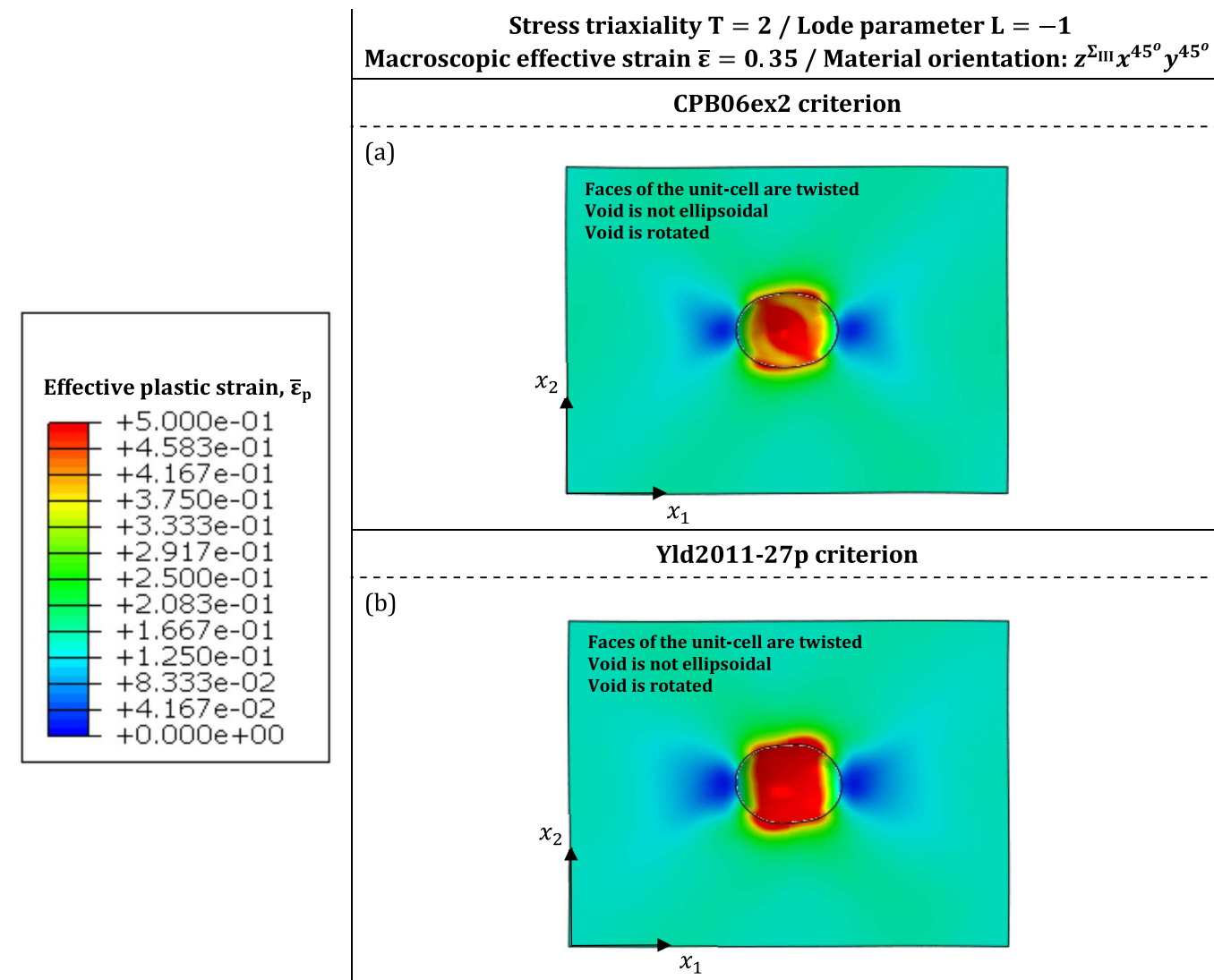


Figure A.29: Influence of the constitutive model on void growth for AA 2090-T3. Contours of effective plastic strain in the matrix material  $\bar{\epsilon}_p$  for unit-cell finite element calculations performed with macroscopic triaxiality  $T = 2$  and Lode parameter  $L = -1$  (axisymmetric tension). Cut-view for  $x_2 = L_0/2$ . The macroscopic effective strain is  $\bar{\epsilon} = 0.35$ . Calculations carried out for material orientation  $z^{\Sigma_{III}} x^{45^\circ} y^{45^\circ}$  with: (a) CPB06ex2 yield criterion (Plunkett et al., 2008) and (b) Yld2011-27p yield criterion (Aretz and Barlat, 2013).

699 **References**

- 700 ABAQUS/Standard, 2016. ABAQUS/Standard User's Manual. version 6.19 ed., Dassault Systèmes, Providence, USA.
- 701 Abedrabbo, N., Pourboghrat, F., Carsley, J., 2007. Forming of AA5182-O and AA5754-O at elevated temperatures  
702 using coupled thermo-mechanical finite element models. *International Journal of Plasticity* 23, 841 – 875.
- 703 Achani, D., Hopperstad, O.S., Lademo, O.G., 2009. Influence of advanced yield criteria on predictions of plastic  
704 anisotropy for aluminium alloy sheets. *International Journal of Material Forming* 2, 487–490.
- 705 Achani, D., Lademo, O.G., Engler, O., Hopperstad, O.S., 2011. Evaluation of constitutive models for textured aluminium  
706 alloys using plane-strain tension and shear tests. *International Journal of Material Forming* 4, 227–241.
- 707 Aretz, H., Barlat, F., 2013. New convex yield functions for orthotropic metal plasticity. *International Journal of*  
708 *Non-Linear Mechanics* 51, 97 – 111.
- 709 Banabic, D., Barlat, F., Cazacu, O., Kuwabara, T., 2000. Advances in anisotropy and formability. *International Journal*  
710 *of Material Forming* 3, 165–189.
- 711 Barber, C.B., Dobkin, D.P., Huhdanpaa, H., 1996. The quickhull algorithm for convex hulls 22, 469–483.
- 712 Barlat, F., Aretz, H., Yoon, J.W., Karabin, M.E., Brem, J.C., Dick, R.E., 2005. Linear transformation-based anisotropic  
713 yield functions. *International Journal of Plasticity* 21, 1009 – 1039.
- 714 Barlat, F., Becker, R.C., Hayashida, Y., Maeda, Y., Yanagawa, M., Chung, K., Brem, J.C., Lege, D.J., Matsui, K.,  
715 Murtha, S.J., Hattori, S., 1997. Yielding description for solution strengthened aluminum alloys. *International Journal*  
716 *of Plasticity* 13, 385 – 401.
- 717 Barlat, F., Brem, J.C., Yoon, J.W., Chung, K., Dick, R.E., Lege, D.J., Pourboghrat, F., Choi, S.H., Chu, E., 2003.  
718 Plane stress yield function for aluminum alloy sheets—Part I: theory. *International Journal of Plasticity* 19, 1297 –  
719 1319.
- 720 Barlat, F., Lege, D.J., Brem, J.C., 1991. A six-component yield function for anisotropic materials. *International Journal*  
721 *of Plasticity* 7, 693–712.
- 722 Barlat, F., Lian, K., 1989. Plastic behavior and stretchability of sheet metals. Part I: A yield function for orthotropic  
723 sheets under plane stress conditions. *International Journal of Plasticity* 5, 51 – 66.
- 724 Basu, S., Dogan, E., Kondori, B., Karaman, I., Benzerga, A.A., 2017. Towards designing anisotropy for ductility  
725 enhancement: A theory-driven investigation in Mg-alloys. *Acta Materialia* 131, 349–362.

- 726 Becker, R., Callaghan, K., 2020. Void growth dependence on loading path and mean stress from large-scale numerical  
727 simulations. *International Journal of Plasticity* 134, 102780.
- 728 Becker, R., Smelser, R.E., 1994. Simulation of strain localization and fracture between holes in an aluminum sheet.  
729 *Journal of the Mechanics and Physics of Solids* 42, 773 – 796.
- 730 Benzerga, A.A., Besson, J., 2001. Plastic potentials for anisotropic porous solids. *European Journal of Mechanics -*  
731 *A/Solids* 20, 397 – 434.
- 732 Benzerga, A.A., Besson, J., Pineau, A., 2004a. Anisotropic ductile fracture: Part I: experiments. *Acta Materialia* 52,  
733 4623 – 4638.
- 734 Benzerga, A.A., Besson, J., Pineau, A., 2004b. Anisotropic ductile fracture: Part II: theory. *Acta Materialia* 52, 4639  
735 – 4650.
- 736 Benzerga, A.A., Leblond, J.B., 2010. Ductile fracture by void growth to coalescence, in: Aref, H., van der Giessen, E.  
737 (Eds.), *Advances in Applied Mechanics*. Elsevier. volume 44 of *Advances in Applied Mechanics*, pp. 169 – 305.
- 738 Benzerga, A.A., Thomas, N., Herrington, J.S., 2019. Plastic flow anisotropy drives shear fracture. *Scientific Reports* 9,  
739 1425.
- 740 Bron, F., Besson, J., 2004. A yield function for anisotropic materials. application to aluminum alloys. *International*  
741 *Journal of Plasticity* 20, 937 – 963.
- 742 Brünig, M., Gerke, S., Schmidt, M., 2018. Damage and failure at negative stress triaxialities: Experiments, modeling  
743 and numerical simulations. *International Journal of Plasticity* 102, 70–82.
- 744 Bryhni Dæhli, L.E., Faleskog, J., Børvik, T., Hopperstad, O.S., 2017a. Unit cell simulations and porous plasticity  
745 modelling for strongly anisotropic FCC metals. *European Journal of Mechanics - A/Solids* 65, 360 – 383.
- 746 Bryhni Dæhli, L.E., Morin, D., Børvik, T., Hopperstad, O.S., 2017b. Influence of yield surface curvature on the  
747 macroscopic yielding and ductile failure of isotropic porous plastic materials. *Journal of the Mechanics and Physics*  
748 *of Solids* 107, 253 – 283.
- 749 Cao, T.S., Maziere, M., Danas, K., Besson, J., 2015. A model for ductile damage prediction at low stress triaxialities  
750 incorporating void shape change and void rotation. *International Journal of Solids and Structures* 63, 240 – 263.
- 751 Chien, W.Y., Pan, J., Tang, S.C., 2001. Modified anisotropic gurson yield criterion for porous ductile sheet metals.  
752 *Journal of Engineering Materials and Technology* 123, 409–413.

- 753 Cvitanić, V., Vlak, F., Lozina, Ž., 2008. A finite element formulation based on non-associated plasticity for sheet metal  
754 forming. *International Journal of Plasticity* 24, 646 – 687.
- 755 Dakshinamurthy, M., Kowalczyk-Gajewska, K., Vadillo, G., 2021. Influence of crystallographic orientation on the void  
756 growth at the grain boundaries in bi-crystals. *International Journal of Solids and Structures* 212, 61 – 79.
- 757 Danas, K., Ponte Castañeda, P., 2012. Influence of the lode parameter and the stress triaxiality on the failure of  
758 elasto-plastic porous materials. *International Journal of Solids and Structures* 49, 1325 – 1342.
- 759 Faleskog, J., Gao, X., Shih, C.F., 2000. Cell model for nonlinear fracture analysis - I. Micromechanics calibration.  
760 *Journal of the Mechanics and Physics of Solids* 89, 355–373.
- 761 Fourmeau, M., Børvik, T., Benallal, A., Hopperstad, O.S., 2013. Anisotropic failure modes of high-strength aluminium  
762 alloy under various stress states. *International Journal of Plasticity* 48, 34 – 53.
- 763 Fourmeau, M., Børvik, T., Benallal, A., Lademo, O.G., Hopperstad, O.S., 2011. On the plastic anisotropy of an  
764 aluminium alloy and its influence on constrained multiaxial flow. *International Journal of Plasticity* 27, 2005 – 2025.  
765 Special Issue In Honor of Nobutada Ohno.
- 766 Frodal, B.H., Bryhni Dæhli, L.E.L.E., Børvik, T., Hopperstad, O.S., 2019. Modelling and simulation of ductile failure in  
767 textured aluminium alloys subjected to compression-tension loading. *International Journal of Plasticity* 118, 36–69.
- 768 Frodal, B.H., Morin, D., Børvik, T., Hopperstad, O.S., 2020. On the effect of plastic anisotropy, strength and work  
769 hardening on the tensile ductility of aluminium alloys. *International Journal of Solids and Structures* 188-189, 118–132.
- 770 Garrison, W.M., Moody, N.R., 1987. Ductile fracture. *Journal of Physics and Chemistry of Solids* 48, 1035 – 1074.
- 771 Gurson, A., 1977. Continuum theory of ductile rupture by void nucleation and growth. Part I: Yield criteria and flow  
772 rules for porous ductile media. *Journal of Engineering Materials and Technology* 99, 2–15.
- 773 Ha, J., Baral, M., Korkolis, Y.P., 2018. Plastic anisotropy and ductile fracture of bake-hardened aa6013 aluminum  
774 sheet. *International Journal of Solids and Structures* 155, 123–139.
- 775 Han, X., Besson, J., Forest, S., Tanguy, B., Bugat, S., 2013. A yield function for single crystals containing voids.  
776 *International Journal of Solids and Structures* 50, 2115 – 2131.
- 777 Hershey, A.V., 1954. The plasticity of an isotropic aggregate of anisotropic face centered cubic crystals. *Journal of*  
778 *Applied Mechanics* 76, 241–249.

- 779 Hill, R., 1948. A theory of the yielding and plastic flow of anisotropic metals, in: Proceedings of the Royal Society of  
780 London A: Mathematical, Physical and Engineering Sciences, The Royal Society. pp. 281–297.
- 781 Hill, R., 1979. Theoretical plasticity of textured aggregates. *Mathematical Proceedings of the Cambridge Philosophical*  
782 *Society* 85, 179–191.
- 783 Hill, R., 1993. A user-friendly theory of orthotropic plasticity in sheet metals. *International Journal of Mechanical*  
784 *Sciences* 35, 19 – 25.
- 785 Hosford, W.F., 1972. A Generalized Isotropic Yield Criterion. *Journal of Applied Mechanics* 39, 607–609.
- 786 Hosseini, N., Rodríguez-Martínez, J.A., 2021. A simple and computationally efficient stress integration scheme based  
787 on numerical approximation of the yield function gradients: Application to advanced yield criteria. *Finite Elements*  
788 *in Analysis & Design* 192.
- 789 Karafillis, A.P., Boyce, M.C., 1993. A general anisotropic yield criterion using bounds and a transformation weighting  
790 tensor. *Journal of the Mechanics and Physics of Solids* 41, 1859 – 1886.
- 791 Keralavarma, S.M., Benzerga, A.A., 2010. A constitutive model for plastically anisotropic solids with non-spherical  
792 voids. *Journal of the Mechanics and Physics of Solids* 58, 874 – 901.
- 793 Keralavarma, S.M., Hoelscher, S., Benzerga, A.A., 2011. Void growth and coalescence in anisotropic plastic solids.  
794 *International Journal of Solids and Structures* 48, 1696 – 1710.
- 795 Khadyko, M., Dumoulin, S., Børvik, T., Hopperstad, O.S., 2014. An experimental–numerical method to determine  
796 the work-hardening of anisotropic ductile materials at large strains. *International Journal of Mechanical Sciences* 88,  
797 25–36.
- 798 Khadyko, M., Morin, D., Børvik, T., Hopperstad, O.S., 2019. Tensile ductility of extruded aluminium alloy AA6063 in  
799 different temps. *Materials Science and Engineering: A* 744, 500–511.
- 800 Kim, D., Lee, W., Kim, J., Kim, C., Chung, K., 2010. Formability evaluation of friction stir welded 6111-T4 sheet with  
801 respect to joining material direction. *International journal of mechanical sciences* 52, 612–625.
- 802 Kim, J., Gao, X., Srivatsan, T.S., 2004. Modeling of void growth in ductile solids: effects of stress triaxiality and initial  
803 porosity. *Engineering Fracture Mechanics* 71, 379 – 400.
- 804 Koplik, J., Needleman, A., 1988. Void growth and coalescence in porous plastic solids. *International Journal of Solids*  
805 *and Structures* 24, 835 – 853.

- 806 Kuna, M., Sun, D.Z., 1994. Three-dimensional cell model analyses of void growth in ductile materials. *International*  
807 *Journal of Fracture* 81, 235–258.
- 808 Lebensohn, R.A., Cazacu, O., 2012. Effect of single-crystal plastic deformation mechanisms on the dilatational plastic  
809 response of porous polycrystals. *International Journal of Solids and Structures* 49, 3838 – 3852.
- 810 Leblond, J.B., Mottet, G., 2008. A theoretical approach of strain localization within thin planar bands in porous ductile  
811 materials. *Comptes Rendus Mécanique* 336, 176 – 189. Duality, inverse problems and nonlinear problems in solid  
812 mechanics.
- 813 Legarth, B.N., Tvergaard, V., 2018. Effects of plastic anisotropy and void shape on full three-dimensional void growth.  
814 *Journal of Applied Mechanics* 85(5), 051007.
- 815 Maire, E., Zhou, S., Adrien, J., Dimichiel, M., 2011. Damage quantification in aluminium alloys using in situ tensile  
816 tests in x-ray tomography. *Engineering Fracture Mechanics* 78, 2679 – 2690.
- 817 McVeigh, C., Vernerey, F., Liu, W.K., Moran, B., Olson, G., 2007. An interactive micro-void shear localization mecha-  
818 nism in high strength steels. *Journal of the Mechanics and Physics of Solids* 55, 225 – 244.
- 819 Mises, R.V., 1913. *Nachrichten von der gesellschaft der wissenschaften zu göttingen. Mathematisch-Physikalische Klasse*  
820 , 582.
- 821 Mises, R.V., 1928. *Mechanik der plastischen formänderung von kristallen. ZAMM - Journal of Applied Mathematics*  
822 *and Mechanics / Zeitschrift für Angewandte Mathematik und Mechanik* 8, 161–185.
- 823 Nasim, W., Herrington, J.S., Benzerga, A.A., Wang, J., Karaman, I., 2019. Inverse optimization to design processing  
824 paths to tailor formability of mg alloys, in: Joshi, V.V., Jordon, J.B., Orlov, D., Neelameggham, N.R. (Eds.),  
825 *Magnesium Technology 2019*, Springer International Publishing, Cham. pp. 239–246.
- 826 Needleman, A., 1972. Void Growth in an Elastic-Plastic Medium. *Journal of Applied Mechanics* 39, 964–970.
- 827 Nielsen, K.L., Dahl, J., Tvergaard, V., 2012. Collapse and coalescence of spherical voids subject to intense shearing:  
828 studied in full 3D. *International Journal of Fracture* 17, 97–108.
- 829 Pardoen, T., Hutchinson, J.W., 2000. An extended model for void growth and coalescence. *Journal of the Mechanics*  
830 *and Physics of Solids* 48, 2467 – 2512.
- 831 Pardoen, T., Hutchinson, J.W., 2003. Micromechanics-based model for trends in toughness of ductile metals. *Acta*  
832 *Materialia* 51, 133 – 148.

- 833 Plunkett, B., Cazacu, O., Barlat, F., 2008. Orthotropic yield criteria for description of the anisotropy in tension and  
834 compression of sheet metals. *International Journal of Plasticity* 24, 847–866.
- 835 Reboul, J., Srivastava, A., Osovski, S., Vadillo, G., 2020. Influence of strain rate sensitivity on localization and void  
836 coalescence. *International Journal of Plasticity* 125, 265–279.
- 837 Rice, J.R., Tracey, D.M., 1969. On the ductile enlargement of voids in triaxial stress fields. *Journal of the Mechanics  
838 and Physics of Solids* 17, 201 – 217.
- 839 Scheyvaerts, F., Onck, P., Lu, C.T., Pardoën, T., 2011. The growth and coalescence of ellipsoidal voids in plane strain  
840 under combined shear and tension. *Journal of the Mechanics and Physics of Solids* 59, 373 – 397.
- 841 Shen, W.Q., Shao, J.F., Liu, Z.B., Oueslati, A., De Saxcé, G., 2020. Evaluation and improvement of macroscopic yield  
842 criteria of porous media having a drucker-prager matrix. *International Journal of Plasticity* 126, 102609.
- 843 Srivastava, A., Needleman, A., 2015. Effect of crystal orientation on porosity evolution in a creeping single crystal.  
844 *Mechanics of Materials* 90, 10 – 29. *Proceedings of the IUTAM Symposium on Micromechanics of Defects in Solids*.
- 845 Steglich, D., Wafai, H., Besson, J., 2010. Interaction between anisotropic plastic deformation and damage evolution in  
846 Al 2198 sheet metal. *Engineering Fracture Mechanics* 77, 3501 – 3518.
- 847 Tardif, N., Kyriakides, S., 2012. Determination of anisotropy and material hardening for aluminum sheet metal.  
848 *International Journal of Solids and Structures* 49, 3496 – 3506. *New Challenges in Mechanics & Materials for Sheet  
849 Metal Forming*.
- 850 Tekoğlu, C., Hutchinson, J., Pardoën, T., 2015. On localization and void coalescence as a precursor to ductile fracture.  
851 *Philosophical Transactions of the Royal Society A: Mathematical, Physical and Engineering Sciences* 373, 20140121.
- 852 Toda, H., Sinclair, I., Buffière, J.Y., Maire, E., Khor, K., Gregson, P., Kobayashi, T., 2004. A 3D measurement  
853 procedure for internal local crack driving forces via synchrotron X-ray microtomography. *Acta Materialia* 52, 1305 –  
854 1317.
- 855 Torki, M.E., 2019. A unified criterion for void growth and coalescence under combined tension and shear. *International  
856 Journal of Plasticity* 119, 57–84.
- 857 Torki, M.E., Tekoğlu, C., Leblond, J.B., Benzerga, A.A., 2017. Theoretical and numerical analysis of void coalescence  
858 in porous ductile solids under arbitrary loadings. *International Journal of Plasticity* 91, 160–181.

- 859 Tvergaard, V., 1982. On localization in ductile materials containing spherical voids. *International Journal of Fracture*  
860 18, 237–252.
- 861 Tvergaard, V., 1990. Material failure by void growth to coalescence. *Advances in Applied Mechanics* 27, 83–151.
- 862 Tvergaard, V., 2015. Effect of initial void shape on ductile failure in a shear field. *Mechanics of Materials* 90, 2 – 9.  
863 Proceedings of the IUTAM Symposium on Micromechanics of Defects in Solids.
- 864 Vadillo, G., Reboul, J., Fernández-Sáez, J., 2016. A modified gurson model to account for the influence of the lode  
865 parameter at high triaxialities. *European Journal of Mechanics - A/Solids* 56, 31 – 44.
- 866 Wan, J.S., Yue, Z.F., Lu, Z.Z., 2005. Casting microporosity growth in single-crystal superalloys by a three-dimensional  
867 unit cell analysis. *Modelling and Simulation in Materials Science and Engineering* 13, 875–892.
- 868 Wang, D.A., Pan, J., Liu, S.D., 2004. An anisotropic gurson yield criterion for porous ductile sheet metals with planar  
869 anisotropy. *International Journal of Damage Mechanics* 13, 7–33.
- 870 Worswick, M.J., Pick, R.J., 1990. Void growth and constitutive softening in a periodically voided solid. *Journal of the*  
871 *Mechanics and Physics of Solids* 38, 601 – 625.
- 872 Yerra, S.K., Ilu, C.T., Scheyvaerts, F., Delannay, L., Van Houtte, P., Pardoën, T., 2010. Void growth and coalescence  
873 in single crystals. *International Journal of Solids and Structures* 47, 1016 – 1029.
- 874 Yoon, J.W., Barlat, F., Dick, R.E., Karabin, M.E., 2006. Prediction of six or eight ears in a drawn cup based on a new  
875 anisotropic yield function. *International Journal of Plasticity* 22, 174 – 193.
- 876 Zhang, K.S., Bai, J.B., François, D., 2001. Numerical analysis of the influence of the lode parameter on void growth.  
877 *International Journal of Solids and Structures* 38, 5847 – 5856.